Received June 2, 2020, accepted June 7, 2020, date of publication June 12, 2020, date of current version July 2, 2020.

Digital Object Identifier 10.1109/ACCESS.2020.3002183

Absorption of 5G Radiation in Brain Tissue as a Function of Frequency, Power and Time

DAVID H. GULTEKIN[1,2] AND PETER H. SIEGEL[2,3,4], (Life Fellow, IEEE)

[1]Zuckerman Mind Brain Behavior Institute, Columbia University, New York City, NY 10027, USA
[2]THz Global, La Cañada Flintridge, CA 91011, USA
[3]Jet Propulsion Laboratory, National Aeronautics and Space Administration, Pasadena, CA 91109, USA
[4]Department of Electrical Engineering, California Institute of Technology, Pasadena, CA 91125, USA

Corresponding authors: David H. Gultekin (dg3155@columbia.edu) and Peter H. Siegel (phs@caltech.edu)

This work was supported by THz Global.

ABSTRACT The rapid release of 5G wireless communications networks has spurred renewed concerns regarding the interactions of higher radiofrequency (RF) radiation with living species. We examine RF exposure and absorption in ex vivo bovine brain tissue and a brain simulating gel at three frequencies: 1.9 GHz, 4 GHz and 39 GHz that are relevant to current (4G), and upcoming (5G) spectra. We introduce a highly sensitive thermal method for the assessment of radiation exposure, and derive experimentally, accurate relations between the temperature rise (ΔT), specific absorption rate (SAR) and the incident power density (F), and tabulate the coefficients, $\Delta T/\Delta F$ and $\Delta(\text{SAR})/\Delta F$, as a function of frequency, depth and time. This new method provides both ΔT and SAR applicable to the frequency range below and above 6 GHz as shown at 1.9, 4 and 39 GHz, and demonstrates the most sensitive experimental assessment of brain tissue exposure to millimeter-wave radiation to date, with a detection limit of 1 mW. We examine the beam penetration, absorption and thermal diffusion at representative 4G and 5G frequencies and show that the RF heating increases rapidly with frequency due to decreasing RF source wavelength and increasing power density with the same incident power and exposure time. We also show the temperature effects of continuous wave, rapid pulse sequences and single pulses with varying pulse duration, and we employ electromagnetic modeling to map the field distributions in the tissue. Finally, using this new methodology, we measure the thermal diffusivity of ex vivo bovine brain tissue experimentally.

INDEX TERMS 4G, 5G, microwaves, millimeter-waves, wireless, RF absorption, RF safety, RF heating, bovine brain tissue, Triton gel.

I. RESEARCH MOTIVATION

There is an increasing trend to implement information and communications technologies with much higher data transmission rates. More than half of the world's population is now online, and nearly the entire world population is within the reach of a mobile cellular network [1], [2]. The forthcoming fifth generation (5G) wireless communications system will extend the existing networks beyond the already nearly seven billion current cell phone users and into the realm of the Internet of Things, potentially linking trillions of wireless devices [1], [2]. The identified 5G use cases are based largely on enhanced mobile broadband, massive machine-to-machine communications and ultra-reliable and low latency communications [1], [2]. The strategic importance of such extensive information and communications technologies has set up an intense international competition for acquiring the all-embracing infrastructure with strong implications for economic growth, defense and national security [3]–[5].

The overall data capacity depends on the cell density, spectral efficiency and frequency bandwidth. Current technical performance requirements need both new radio broadcast technologies and much broader spectrum [1], [2]. A preferred method for realizing the spectrum requirements is to use higher frequencies, specifically the millimeter-wave bands between 30 and 300 GHz. Also, increasing the frequency and decreasing the corresponding wavelength allows for miniaturization of antennas, base stations and wireless-enabled devices, making them more suitable for enhancing the cell density. However, millimeter waves have short ranges of propagation, they are absorbed by water vapor and oxygen in the atmosphere, by vegetation, very strongly by water

The associate editor coordinating the review of this manuscript and approving it for publication was Derek Abbott.

in the tissues of people and animals, and they are readily reflected off, and scattered by, small metallic and dielectric objects, urban clutter and large manmade and natural structures [6]–[8]. Overcoming these limitations by increasing the cell density, increases cell interference and necessitates higher directivity and hence higher power density. Increasing the frequency and bandwidth requires significant spectral fencing at the expense of other applications.

Currently, the sub-6 GHz spectrum is very crowded, and already includes 3G/4G cellular, GPS, Wi-Fi, L-band satellite, S-band and C-band radars and other allocations. In order to reduce the interference and power requirements, and to improve the range and spectral efficiency, one solution for 5G is network densification, which employs a massive number of smaller cells and a massive number of smaller antennas in each base station with high directivity electronic beam forming and steering capabilities [9]. The number of transmit and receive antennas per base station will typically increase with increasing frequency for indoor hotspots as well as to enable dense urban and rural mobile broadband coverage. Upcoming mobile communication networks will use multiband radios with a combination of low, mid and high band frequencies to optimize the coverage and capacity [10]. As of today, the allocated bands have been broadly specified as below or above 6 GHz and labeled as: low-band (600, 800 and 900 MHz); mid-band (2.5, 3.5 and 3.7-4.2 GHz); and high-band (24, 26, 28, 37, 39, 42 and 47 GHz) with remaining unlicensed bands above 95 GHz [10].

Despite standards set by the FCC and RF communities, absorption of electromagnetic radiation in biological tissues has been, and continues to be, a public concern [11]–[16]. This will become more so with the upcoming deployment of large numbers of higher frequency and higher power devices with increased directionality as 5G rolls out. Some of the relevant early studies have tried to accurately assess biological interactions and effective absorption rates of high frequency RF with both humans and animal models [17]–[38].

There are also ongoing studies that assess the established guidelines [39], [40] for exposure to the upcoming 5G high frequency bands. Recently, the International Commission on Non-Ionizing Radiation Protection (ICNIRP) revised their guidelines and the Institute of Electrical and Electronics Engineers (IEEE) revised the C95.1 standard so as to use the specific absorption rate (SAR) below 6 GHz and absorbed power density (PD) above 6 GHz [39], [40]. The current approaches taken generally, use direct measurement of radiation from the transmitting devices through a probe moving in a three-dimensional grid in a tissue simulating fluid [41] or use modeling and software simulations to predict SAR in biological media [42]. Although, the research community continues to debate between thermal and nonthermal effects of absorbed radiation at particular SAR levels [43], we propose that such distinctions may essentially be related to the detection limits of absorption in biological tissue at very low levels. Once an accurate dependence of the thermal constants and mechanisms are established, it is possible to accurately estimate the absorption at very low RF power levels. Setting such thresholds would then no longer be a subject of debate. Ultimately, the temperature effects on physical, chemical, electrochemical and biological processes are complex and may register as positive, negative or null effects in specific tissues or organisms [44], [45].

Despite the controversies over studies of existing wireless systems up to 1.9 GHz (4G), the beam penetration, absorption and thermal diffusion effects of millimeter-waves (5G) in tissues differ significantly from 4G values. Although, it is common to extrapolate lower frequency absorption and temperature rise by relying on pre-measured tissue dielectric characteristics and electromagnetic models to set safety requirements throughout the millimeter-wave bands, such models do not generally take into account detailed RF beam characteristics, thermal diffusion and convection, or specific exposure geometries and conditions. We believe there is both a clear need, and a lot to learn by introducing simple experimental methods that extend the lower frequency investigations on specific tissues over the entire 5G frequency range.

II. INTRODUCTION TO THIS STUDY

In earlier work, the effects of microwave radiation on the brain metabolic activities in human volunteers exposed to cell phone radiation were studied in vivo by Positron Emission Tomography (PET) [46], and we studied, by Magnetic Resonance Imaging (MRI), the absorption characteristics of 1.9 GHz radiation in ex vivo bovine brain tissue exposed to a realistic cell phone antenna by measuring the temperature as a function of power and exposure time [47]. Cell damage and cell death rate are a function of temperature and time of the exposure [48], [49]. There is a growing interest in using the temperature-time diagrams and thermal dosimetry to assess power absorption in biological tissue as a measure of safety. The SAR varies spatially and temporally in the tissue and it often requires averaging over a prescribed mass or volume. The measurement of SAR by thermal methods is also complicated and it requires the determination of thermal transport parameters [47], [50]–[52] to assess SAR accurately.

In this paper, we extend and compare our earlier 1.9 GHz study [47] and characterize the fundamentals of absorption and subsequent heating of both microwave and millimeter-wave radiation in ex vivo bovine brain tissue and a gel simulant as a function of frequency, power, exposure time, and penetration depth at 1.9 GHz (overlap with 4G), 4 GHz (lower end of the 5G band) and 39 GHz (high end of the 5G band). We use a very simple and flexible test system with accurately characterized, single mode rectangular waveguide RF power insertion, which has well-defined and well-confined beam characteristics. We introduce an easy to implement, and very accurate tissue embedded thermal measurement method, capable of measuring both temperature rise (ΔT) and specific absorption rate (SAR) versus incident power density (F), universally applicable to the entire 4G and 5G frequency range without making the distinctions below and above 6 GHz.

There have been a number of prior studies in the microwave and millimeter-wave bands on the dielectric properties of brain tissue [53]–[56], tissue and head modeling [57]–[60] and RF energy exposure modeling [61]–[68]. Here, we study simultaneously the effects of beam penetration, absorption and thermal diffusion in brain tissue through real-time temperature measurements during the irradiation. This study provides a broad range of experimental measurements in the tissue that can be useful for computational RF exposure modeling and simulations.

We derive experimentally very accurate thermal coefficients ($\Delta T/\Delta F$ and $\Delta(\mathrm{SAR})/\Delta F$) versus frequency and depth in the tissue, and correlate with well-defined RF beam pattern distribution and penetration. We believe that our very carefully calibrated temperature versus depth profiles, well-defined RF beam patterns and incident power density values, and simple and flexible RF test system are unique but widely applicable. Our experimentally derived and tabulated $\Delta T/\Delta F$ and $\Delta(\mathrm{SAR})/\Delta F$ coefficients at each frequency can be used to assess the magnitude of heating and specific absorption rate at any depth given the power exposure, even to values which would normally be below measurable levels using standard thermal sensors. We show that the use of common gel simulants that have been employed for 4G experiments are applicable only over a low range of power and exposure time for 5G frequency bands, especially in the millimeter-wave range.

We also show experimentally, the effects of rapid pulsing of the RF power at different pulse lengths (1 μs, 1 ms and 1 s) at 50% duty cycle in the gel and single pulses of short (1 s) and long (30 s) duration with on/off RF cycles in both brain tissue and gel. Using our measurements here and our prior MRI studies to derive thermal parameters [47], [50], [51], [69], [70], we derive an accurate thermal diffusivity coefficient for the ex vivo bovine brain tissue. These measurements are supported by finite difference time domain simulations (Appendix) showing in detail, the distribution of RF source power with depth and surface area in the tissue.

III. DETAILED EXPERIMENTAL METHODS

A compact and frequency agile experimental system was designed to study the absorption of electromagnetic waves in ex vivo brain and brain equivalent gels as a function of power, frequency and exposure time. Fig. 1 shows the experimental setup. The brain and gel samples were contained in thin wall cubic plastic Poly(methyl methacrylate) (PMMA) containers and illuminated with RF through the container walls using standard TE_{10} mode rectangular waveguides. The sample temperature was monitored axially along the center of the waveguide aperture with inserted thermocouples housed in glass capillary tubes. The incident microwave power was precalibrated at the waveguide output and derived from a variety of synthesized continuous wave sources and power amplifiers that were connected to the waveguides through coaxial cable. Since the brain tissue and gel samples have no preferential polarization direction at these wavelengths [19], [25], [26],

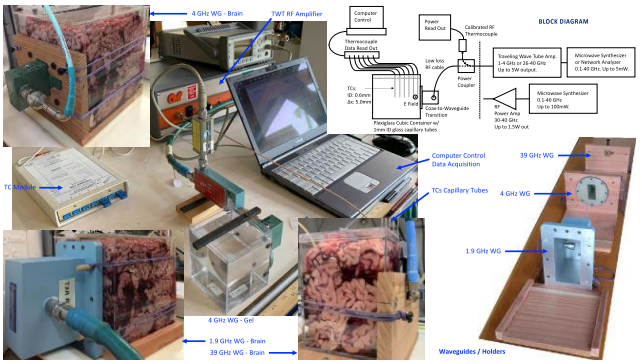

FIGURE 1. Experimental setup showing the waveguides (1.9, 4 and 39 GHz), specially fabricated wooden holders, plexiglass cubes containing brain and gel, thermocouples, signal generators and radiofrequency amplifiers.

[71], [72], the waveguides were always oriented so that the electric field had minimal coupling to the embedded thermocouple wires. Specific details for each exposure frequency follow the sample descriptions.

For this study, three single mode rectangular waveguides (WR) with internal dimensions (ID) and aperture areas (A) (WR-430, pass band 1.7-2.6 GHz, ID: 109.2 × 54.6 mm, A: 5962.3 mm^2; WR-187, pass band 3.95-5.85 GHz, ID: 47.5 × 22.1 mm, A: 1049.8 mm^2; and WR-28, pass band 26.5-40 GHz, ID: 7.1 × 3.6 mm, A: 25.6 mm^2) were used for beam forming and directing the microwave power into the medium in a well determined exposure pattern (see Appendix). The waveguides were operated at frequencies of 1.9 GHz, 4 GHz and 39 GHz corresponding to wavelengths of 157.8 mm, 74.9 mm and 7.7 mm, respectively. They were held tightly, and in a predetermined position, against the sample cubes using rubber bands and wooden (low thermal constant) positioning jigs. The waveguide E-field was oriented so that it was always perpendicular to the plane of the embedded thermocouple wires, and no coupling of RF power to the wires themselves was detectable. The thermocouple tips were positioned at the end of their glass capillary tube holders and aligned to the axial center of the different waveguides.

Depending on the aperture size of the waveguides, three different PMMA plastic cubes were utilized. At 1.9 GHz, a cube with ID: 147 × 147 × 147 mm and 3 mm wall thickness, held the gel and required a total of 7 individual bovine brains each of which was approximately 450 g. A cube, with ID: 96 × 96 × 124 mm and 2.25 mm wall thickness, was used for the gel and the brain at 4 GHz and 39 GHz. This cube was filled by approximately 3 bovine brains. Also, a cube, with ID: 84 × 84 × 109 mm and 1.9 mm wall thickness was used just for the gel measurements at 39 GHz at the lower power levels.

The reflection coefficients (R_s) were measured as 0.092, 0.116 and 0.086 for the plastic walls alone, and as 0.47, 0.45 and 0.37 for the plastic walls and brain tissue combined, and using an FDTD simulator, the 10dB power (0.9P), spot

sizes (A_s) on the tissue surface were computed as 5932.80, 1304.16 and 49.60 mm^2 at 1.9, 4 and 39 GHz, respectively. The incident power density (F) on the tissue surface was calculated from the incident power (P) in the waveguide as $F = PR$ where $R = 0.9(1 - R_s)/A_s$ or 137.7, 613.2 and 16577.6 m^{-2} for the three waveguide sources and plastic containers, respectively. If we exclude the plastic wall then $R = 1/A$ or 167.72, 952.61 and 39,123.63 m^{-2} using the aperture areas (A) for the three waveguides. We used the 10dB spot power density on the tissue surface including the plastic walls in our calculations but the results can be scaled using the ratio of the two R values, since the measurement trend is linear with our range of power levels.

The ex vivo bovine brains were used per a specimen permit issued by the United States Department of Agriculture (USDA) Food Safety and Inspection Service (FSIS) in compliance with the Institutional Animal Care and Use Committee (IACUC) and Institutional Review Board (IRB). The brain tissue is classified as specific risk material (SRM) by USDA for bovine spongiform encephalopathy (BSE) or mad cow disease, and was extracted from the animals less than 30 months of age in a local USDA plant, transported to the lab and tested the same day at room temperature in accordance with the USDA, FSIS, IACUC and IRB guidelines. We thought about performing measurements on frozen and thawed samples, to avoid the problem of tissue spoilage when samples were measured over long periods at room temperature. However, when we compared the measured complex dielectric constant of frozen-then-thawed bovine brain, with fresh bovine brain, we saw significant deviations (likely due to water content) and hence were unable to utilize the frozen samples (see Appendix).

A gel formulation (62.7% water, 36.8% Triton X-100 and 0.5% NaCl) was used to compare the radiation from a waveguide to a half-wavelength dipole antenna ($\lambda/2$) at 1.9 GHz in our previous study [47], [73]. This gel is well matched in dielectric properties (index and absorption) to the brain tissue at 1.9 GHz, although it deviates as the frequency increases (see Fig. 11 in Appendix).

Typical radial beam power distribution plots computed using a well vetted commercial finite difference time domain (FDTD) code (Quickwave, QWED Ltd., Warsaw, Poland), are shown in the brain tissue at various thermocouple positions along the waveguide center (See Appendix, Figs. 18-20). The software incorporates measured values for the real and imaginary parts of the refractive index within the brain tissue and includes the plastic sample box. The beam intensity profile in the sample varies approximately as $P(z) = P_0 e^{-\alpha z}$, where z is the distance into the sample in cm, P_0 is the incident power at the surface, and α is the linear absorption coefficient in cm^{-1}. Using the procedure described below, the α values were determined to be 0.46, 0.89 and 23 cm^{-1} for the brain tissue and 0.81, 1.95, and 25.34 cm^{-1} for the gel at 1.9, 4 and 39 GHz respectively, using an Agilent vector network analyzer (PNA 8363B) with a special fringing field coaxial probe (Keysight 85070E) that measures the real and imaginary parts of the dielectric constant over the frequency range 1-40 GHz. Other derived dielectric properties for the samples are given in Table 10 of the Appendix.

For generating the microwave power used to irradiate the samples, a variety of calibrated signal sources were employed at the three frequencies, 1.9, 4 and 39 GHz, depending on the power level required. In all cases a precise synthesized continuous wave signal was employed either directly or as input to a power amplifier. At 1.9 and 4 GHz an HP 8340A (Hewlett Packard) signal generator was coupled to an AR 5SIG4 (AR World) traveling wave tube (TWT) amplifier (maximum output 5W). At 39 GHz, for the gel measurements, one output port of an Agilent 8722ES vector network analyzer was linked to an AR 25T26G40 TWT, and for the brain sample measurements a Keysight E8257D was used along with a custom solid-state Gallium Nitride (GaN) power amplifier supplied by the NASA Jet Propulsion Laboratory. In order to produce the single pulse measurement data, the synthesizer power was manually turned on/off during the experiments in conjunction with a simple timer. For modulated RF power measurements, a separate waveform generator (HP 3312A) was applied to the synthesizer output channel to generate a square wave input signal of the desired length and duty cycle. In all cases, the power output at the waveguide aperture was pre-calibrated using an Agilent 8481A thermocouple power sensor and E4419B display unit to measure the losses in all the utilized cables, coax-to-waveguide converters, attenuators, and connector adapters and wherever possible, monitored during the actual measurements. In some cases, the power levels were too high to directly monitor the RF output of the amplifier, so calibrated attenuators were used to premeasure power levels output from the synthesizer against amplifier output levels, after the amplifier was determined to be in its linear range: $P_{\text{out}}/P_{\text{in}} = \text{constant}$.

An Agilent vector network analyzer and specially designed liquid immersion probe (Keysight 85070E) were used to record the real and imaginary dielectric constant for all the samples between 1 and 40 GHz. A fresh brain sample acquired 1.5 hours before testing was measured along with a sample that had been acquired two weeks earlier, frozen and then thawed for 7 hours at room temperature. The gel and deionized (DI) water samples were also measured, all at 20°C. The dielectric constant measurements, including a comparison of the fresh and frozen-then-thawed bovine brain samples, are shown in Fig. 11 of the Appendix. The measurements also show the correlation between the gel dielectric constant and the brain tissue and where the gel dielectric constant overlaps sufficiently with the brain tissue to be used as a simulant for this particular parameter. The deionized (DI) water was used for calibration of the instrument. These measurements were used to derive the values of electrical conductivity (σ) and linear absorption coefficient (α) that are used in the field computations described earlier, and they are shown in Table 10 of the Appendix at each measurement frequency.

For performing all the measurements, the individual sample containers were filled with gel or fully packed brain tissue, and a rack with five precisely placed thermocouples spaced 5 mm apart was inserted from above, reaching down to positions directly aligned with the waveguide central axis and positioned as 1, 6, 11, 16 and 21 mm away from the inner wall of the container. An additional thermocouple was placed at the center of the container and a glass thermometer was also placed in the far corner of container as an absolute reference. The thermocouples were all type T (Physitemp, NJ, USA) and were either type IT-18 (0.050'' diameter sheathed in Teflon) or IT-23 (0.011'' diameter Teflon coated and twisted). Both are designated for implantation, and they are specially configured for high accuracy (<0.1°C) when used with the Thermes USB (Physitemp) multiprobe module. The reason two types were used was simply due to the availability in our lab – and both varieties were pretested in DI water and shown to give identical readings with temperature and time.

The capillary tubes (Eisco Scientific, LLC part number Bio338A) holding the thermocouple wires were 10 cm long, had an inner diameter of 1 mm and a wall thickness of 0.125 mm and were waxed in place in a wooden slat rack that fits precisely onto the top of the sample container. During the measurements, all the probes were sampled once per second and the thermocouple voltage was converted to temperature and stored in a file on a control laptop using a custom driver (Dasylab, Measurement Computing, USA) that was designed to interface with the Thermes USB module. Pre-calibrated power levels of 1, 2, 4, 8, 16, 32, 62.5, 125, 250, 500, 1000 and 2000 mW were used to irradiate both the brain and gel. Individual measurements consisted of a 5-minute control, 30-minute power on, and 30-minute power off cycle. Since the measurements over all power levels took many hours, the ambient temperature of the room and the sample itself was not constant, and thus this temperature was also recorded through the data acquisition system and glass thermometers placed in the gel and in the air. Any drift relative to the ambient conditions during each approximately one-hour long measurement could then be calibrated out of the datasets.

The system was configured to study the effects of continuous wave (CW) and pulsed exposures. In this case the signal generator on/off power switch was coupled to a waveform generator and pulse lengths (δt) of 1 s, 1 ms and 1 μs with equal duty cycle (on/off = 1) were generated. These three experiments, with a duty cycle of 50% at 2W pulsed power and three pulse lengths, were compared to 1W (CW) applied power at 4 GHz in the gel. Additionally, pulse length effects on temperature rise were studied on all samples using a single pulse with a duration of 1, 2, 3, 4, 5, 10, 20 and 30 s by manually applying RF power (timer and switch) for the given pulse interval and then allowing the sample to cool for a period of 5 minutes before the next pulse was applied.

The 1.9 GHz waveguide was included in this study to compare the results to our previous study, which used a 1.9 GHz $\lambda/2$ dipole antenna for irradiation [47]. The differences between the waveguide and $\lambda/2$ dipole antenna elucidates the varying impact of the RF beam distribution and/or focus and will play a major role in defining standards for 5G base stations which have unprecedented beam forming, directivity, and beam steering characteristics.

For all the data acquired in this study the same sequence was used: 5 minutes without power to acquire a baseline, RF power applied for 30 minutes, RF off for 30 minutes, and then repeated for the next power level in the sequence, running from the lowest to the highest. Pulse measurements were performed at the end of the full power sequence run. The temperature time series were processed for drift correction using the baseline segment of the data by fitting a polynomial function (degree 1-2) depending on the sources of the drift. The temperature-time datasets were segmented into 5 datasets each with 6 minutes long exposure time, and the magnitude of temperature rise was fitted to the applied power density as a function of space and exposure time.

Additionally, a series of measurements in a gel sample in a mid-size container at 29 GHz using power levels from 1 mW to 2000 mW were acquired and compared to the results at 39 GHz in the gel for the same power levels. An analysis of both data sets was performed at the lower levels to avoid thermal convection and both data sets were found to be linear in power vs. temperature over their given exposure time intervals.

IV. RESULTS

The absorption of electromagnetic waves in ex vivo bovine brain and a brain equivalent gel were studied as a function of frequency (f), incident power density (F) and exposure time (t) with a primary goal of measuring accurate temperature (T) and specific absorption rate (SAR) versus incident power density (F) and deriving $\Delta T/\Delta F$ and $\Delta(\mathrm{SAR})/\Delta F$ coefficients for the samples. Three frequency bands, 1.9, 4 and 39 GHz, incident power levels from 1 mW to 2 W (corresponding to incident power densities from 0.14 to 275.40, 0.61 to 1226.40 and 16.58 to 33155.26 W/m^2 at the tissue surface from the three waveguide sources respectively) and exposure times from 1 second to 30 minutes, pulsed and CW, are all presented.

The impinging RF radiation causes complex simultaneous dynamic effects inside the brain tissue as a result of beam penetration, absorption and thermal diffusion, that need to be taken into account to assess the impact of exposure accurately as a function of frequency, power and time. Although, the overall temperature rise is nonlinear with time, it is linear over short intervals, as is the absorbed RF power at discrete exposure times and depths inside the tissue at each frequency we measured. Therefore, we can propose a linear model for temperature change, $dT = (dT/dF)dF$, with power density, and $dT = (dT/dt)dt$ with time, for short exposures. Since SAR is proportional to the initial dT/dt through the specific heat (C), a plot of $C(\Delta T/\Delta t)$ versus F will give a straight line with a slope of $\Delta(\mathrm{SAR})/\Delta F$, and a plot of ΔT versus F will give a slope of $\Delta T/\Delta F$. These incident power density dependent

coefficients of temperature rise and specific absorption rate, $\Delta T/\Delta F$ and $\Delta(\mathrm{SAR})/\Delta F$, can be used as a measure of RF exposure at each frequency and power density range.

The $\Delta T/\Delta F$ can be derived experimentally as a function of frequency, exposure times and depths in the brain tissue after performing a series of high precision temperature vs. depth measurements that span multiple power levels and exposure times at each frequency. The tabulated $\Delta T/\Delta F$ and $\Delta(\mathrm{SAR})/\Delta F$ data can then be used to predict the temperature rise in the brain tissue for any given frequency, incident power density, depth and exposure time at the frequencies, and over the power ranges, we studied. Since we find the $\Delta T/\Delta F$ plots to be linear down to the lowest powers measurable, we believe it is possible to extrapolate $\Delta T/\Delta F$ to power levels below those we can sense with our thermal probes, and to accurately predict even smaller temperature changes in the brain ($<0.1°C$) than we have observed, as a result of even lower RF exposures than we have tested.

We first present the measured temperature rise at each of 5 axial positions within the brain and gel samples as a function of time and incident RF power. All measurements are made at room temperature and any baseline drifts in the thermocouple readings are removed by sampling for 5 minutes without any RF power applied. Power is always applied for 30 minutes, followed by a 30 minute "off" period before the next power level is set and applied. In all cases we moved from the lowest to the highest applied power over a sequence that typically lasts 12 hours for each sample at each frequency.

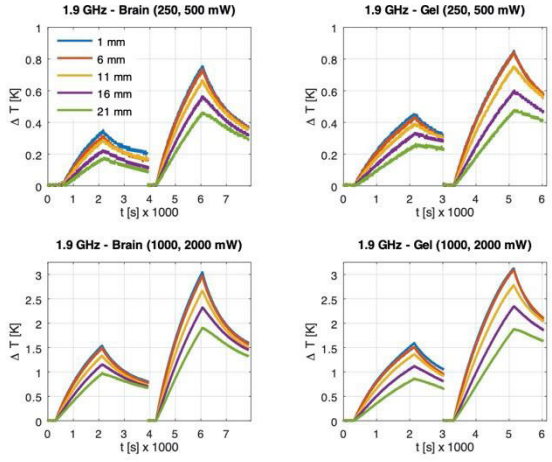

FIGURE 2. Experimental temperature rise (ΔT) vs. time (t) and power (P) for brain (left column) and gel (right column) at 1.9 GHz. The curves correspond to temperature measurements at the power levels of 250, 500, 1000 and 2000 mW and depths of 1, 6, 11, 16 and 21 mm, respectively.

The experimental temperature rise (ΔT) vs. time (t) and incident power (P) for bovine brain (left panel) and gel (right panel) at 1.9 GHz are shown in Fig. 2. The color curves correspond to temperature and time measurements at the power levels of 250, 500, 1000 and 2000 mW, with exposure times of 30 minutes and temperature sampling depths of 1, 6, 11, 16 and 21 mm, respectively.

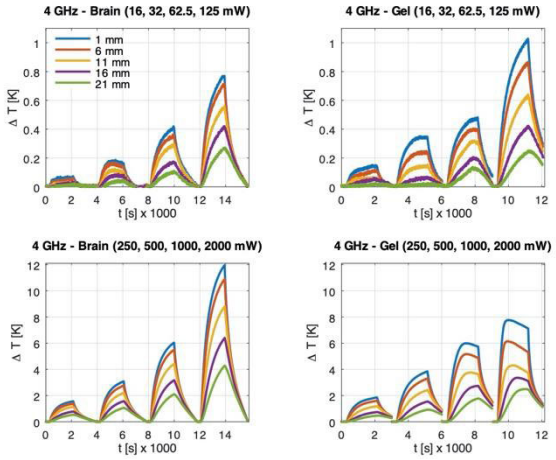

FIGURE 3. Experimental temperature rise (ΔT) vs. time (t) and power (P) for brain (left column) and gel (right column) at 4 GHz. The curves correspond to temperature measurements at the power levels of 16, 32, 62.5, 125, 250, 500, 1000 and 2000 mW and depths of 1, 6, 11, 16 and 21 mm, respectively.

The experimental temperature rise (ΔT) vs. time (t) and incident power (P) for bovine brain (left panel) and gel (right panel) at 4 GHz are shown in Fig. 3. The color curves correspond to temperature and time measurements at the power levels of 16, 32, 62.5, 125, 250, 500, 1000 and 2000 mW, with exposure times of 30 minutes and temperature sampling depths of 1, 6, 11, 16 and 21 mm, respectively. Note that as we move up in frequency, from 1.9 to 4 GHz, and in incident power, the temperature profiles of the brain and gel begin to deviate significantly from one another. This is especially obvious above 1 W, where the gel starts to show thermal convection that indicates a deviation from a strict diffusion model – a flattening, and even thermal rollover, of the peak temperature over time and a rapid cooling when the power is turned off. We conclude that the gel is transitioning to a liquid state at the higher power levels and a convective heating and cooling begins to appear.

The experimental temperature rise (ΔT) vs. time (t) and incident power (P) for bovine brain (left panel) and gel (right panel) at 39 GHz are shown in Fig. 4. The color curves correspond to temperature and time measurements at the power levels of 1, 2, 4, 8, 16, 32, 62.5, 125, 250, 500, 1000 and 2000 mW, with exposure times of 30 minutes and temperature sampling depths of 1, 6, 11, 16 and 21 mm, respectively. Compared to the lower frequency, at 39 GHz the RF heating is higher at every depth while RF absorption is very confined to the surface of the sample (see Appendix) and the resultant rapid changes in the heating and cooling curves are very apparent in both the brain and gel.

At 39 GHz, as at 4 GHz, the brain exhibits a broad range of temperature and power linearity while the gel temperature rise rolls over at high power and the heat transfer appears to have changed over from diffusion to convection. There is now a very large difference between the heating at the first thermocouple (1 mm depth) and the second one (6 mm depth)

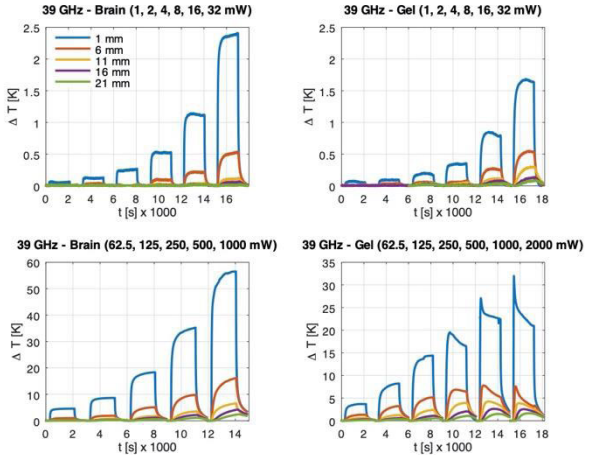

FIGURE 4. Experimental temperature rise (ΔT) vs. time (t) and power (P) for brain (left column) and gel (right column) at 39 GHz. The curves correspond to temperature measurements at the power levels of 1, 2, 4, 8, 16, 32, 62.5, 125, 250, 500, 1000 and 2000 mW and depths of 1, 6, 11, 16 and 21 mm, respectively.

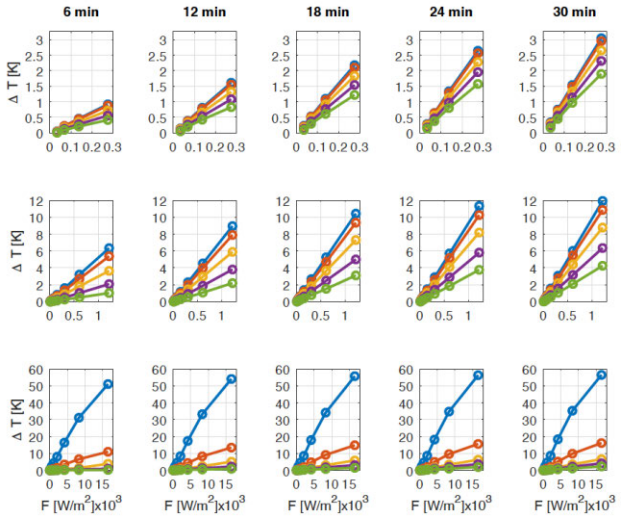

FIGURE 5. Experimental temperature rise (ΔT) vs. incident power density (F), depth (z) and exposure time (t) for brain at 1.9, 4 and 39 GHz. The circles and straight solid lines correspond to temperature measurements and fitted linear functions at exposure times of 6, 12, 18, 24 and 30 min (columns, left to right), and incident power levels of 250 to 2000 mW at 1.9 GHz (top row), 16 to 2000 mW at 4 GHz (middle row) and 1 to 1000 mW at 39 GHz (bottom row) and depths of 1, 6, 11, 16 and 21 mm, respectively.

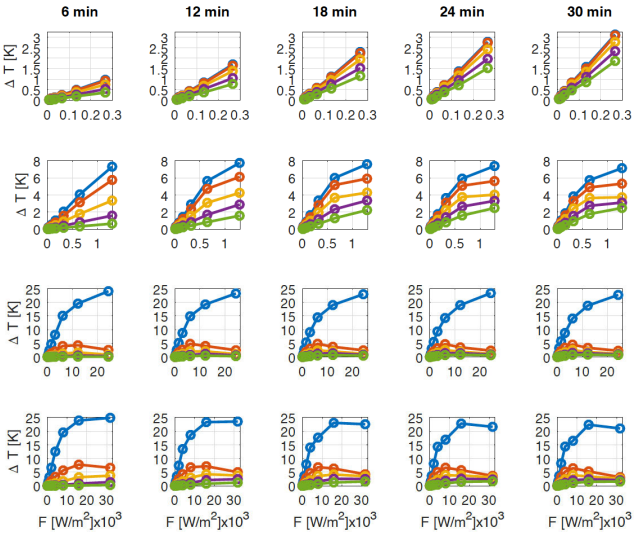

FIGURE 6. Experimental temperature rise (ΔT) vs. incident power density (F), depth (z) and exposure time (t) for gel at 1.9, 4, 29 and 39 GHz. The circles correspond to temperature measurements at exposure times of 6, 12, 18, 24 and 30 min (columns, left to right) and the incident power levels of 62.5 to 2000 mW at 1.9 GHz (top row), 16 to 2000 mW at 4 GHz (second row), 1 to 2000 mW at 29 GHz (third row) and 1 to 2000 mW at 39 GHz (bottom row) and depths of 1, 6, 11, 16 and 21 mm, respectively.

showing much higher thermal gradients. As with the 4 GHz measurements, this shows the confinement of the RF to the surface of the sample and gives a good measure of the thermal time constant for conductive heating in both brain tissue and gel. Note from the top left plot, that we are able to detect very small changes in power (1 mW) and temperature (<0.1°C) in both samples with our setup and our method produces realistic heating profiles even when RF penetration is limited.

As can be seen from Figs 2-4, the magnitude of the temperature rise (ΔT), the temperature rate ($\Delta T/\Delta t$), and the temperature gradient ($\Delta T/\Delta z$), increase rapidly with increasing frequency. The increase in $\Delta T/\Delta z$ in each sample at a given incident power level (P) indicates decreased RF penetration and increased concentration of RF energy near the surfaces as the frequency increases. However, this change is also a function of the thermal diffusion, RF beam concentration, the refractive index at each frequency, and the frequency dependent absorption coefficient, all of which contribute to the position of the most intense RF power in the sample (see Appendix). Although, RF energy density increases near the surface with higher frequency, the heating rate still increases significantly at depth as a result of heat diffusion.

Using the measurement data from Figs. 2-4, we can replot the ΔT vs. ΔF over fixed time intervals and then derive $\Delta T/\Delta F$ for the linear range where a plot of ΔT vs. ΔF has a straight line. The linear range varies with incident power density, frequency and exposure time. These plots are shown in Figs. 5 and 6 for brain and gel at all three frequencies, 1.9, 4 and 39 GHz. Additionally, the gel samples were measured at 29 GHz (Fig. 6).

In Fig. 5, the circles and straight solid lines correspond to temperature measurements and corresponding linear function fits at exposure times of 6, 12, 18, 24 and 30 min (columns) and the power levels of 250 mW to 2 W at 1.9 GHz (top row), 16 mW to 2 W at 4 GHz (middle row) and 1 mW to 1 W at 39 GHz (bottom row) at depths of 1, 6, 11, 16 and 21 mm, respectively. Only power levels that caused measurable ΔT in Figs. 2-4 are used to generate the plots in Fig. 5, hence the higher power range employed at the two lower frequencies. In Fig. 6, the circles correspond to temperature measurements at exposure times of 6, 12, 18, 24 and 30 min (columns) and

incident power levels of 62.5 mW to 2 W at 1.9 GHz (top row), 16 mW to 2 W at 4 GHz (second row), 1 mW to 2 W at 29 GHz (third row) and 1 mW to 2 W at 39 GHz (bottom row) at depths of 1, 6, 11, 16 and 21 mm, respectively. The solid straight lines are fitted functions to the experimental data for the full range of power and exposure times at 1.9 GHz, up to 500 mW for the 4 GHz data and up to 125 mW for the 29 and 39 GHz data.

Fig. 5 shows that the bovine brain tissue exhibits a wide range of linearity in the absorption of RF radiation over a wide range of frequency, power and exposure times. The brain tissue has a linear response up to 2 W in power and up to 30 minutes of exposure time at 1.9 and 4 GHz and up to 1 W at 39 GHz. In contrast, Fig. 6 shows that the temperature and time curves roll over in the gel at the higher powers and 5G frequencies (29 and 39 GHz) especially, at the higher range of power and exposure times. This behavior contrasts dramatically with the bovine brain tissue and is due to changes in the gel properties and onset of convection as a result of severe heating and the concentration of the RF power in the sample (see Appendix).

Overall, the ex vivo bovine brain tissue showed a much wider linear response range than the gel, to power, frequency and exposure time. Over the exposure time of 30 min, fresh brain tissue exhibited perfect linearity up to 2 W at 1.9 and 4 GHz and up to 500 mW at 39 GHz, and near perfect linearity up to 1 W at 39 GHz. The gel showed linearity up to 2 W at 1.9 GHz, up to 500 mW at 4 GHz and only up to 125 mW at 29 and 39 GHz. Both brain and gel showed nonlinear thermal behavior and deformation of temperature profiles due to severe heating beyond their linear limits. Fig. 6 shows that the linear limit is a function of power, frequency and exposure time.

Using the data from Figs. 5 and 6, we have derived a temperature coefficient, $\Delta T/\Delta F$ ($\mathrm{K \cdot m^2/W}$), as a function of frequency (GHz), depth (mm) and exposure time (min) in both the bovine brain and the gel. The individual values are given in Tables 1 and 2 showing mean ± standard deviation. The fitting between the temperature rise and incident power density was performed for exposure times of 6, 12, 18, 24 and 30 min and depths of 1, 6, 11, 16 and 21 mm, respectively. The linear relationship can be extrapolated to much lower power levels so long as the same RF coupling mechanism predominates.

The numbers in the cells in Tables 1 and 2 were derived at spatial distances and exposure times where a linear relation between the temperature (T) and incident power (P), or incident power density (F) dominated. The linearity trend is the same when using T vs. P or T vs. F with a scaling factor R. Using the average incident power (P), and the average incident power density (F), the coefficient $\Delta T/\Delta F$ can be converted to the coefficient $\Delta T/\Delta P$ by multiplying the data in Tables 1 and 2 by the scaling factor (R) of the respective waveguides since $F = PR$ and $\Delta T/\Delta P = R(\Delta T/\Delta F)$. The temperature rise in Kelvin can also be replaced by Celsius since $1\mathrm{K} = 1°\mathrm{C}$.

TABLE 1. Experimental temperature coefficient $\Delta T/\Delta F$ [$\mathrm{K \cdot m^2/W}$] as a function of frequency (GHz), depth (mm) and exposure time (min) for brain. The fitting between the temperature (T) and incident power density (F) was performed over the linear range as $P < 2$W (1.9 and 4GHz) and $P < 0.5$W (39GHz). The results show mean ± standard deviation.

		Brain - $\Delta T/\Delta F$ [$\mathrm{K \cdot m^2/W}$] × 10^{-3}				
f (GHz)	t (min)	1 mm	6 mm	11 mm	16 mm	21 mm
1.9	6	3.51±0.14	3.37±0.20	2.73±0.14	2.18±0.12	1.65±0.10
	12	6.02±0.13	5.82±0.15	4.91±0.12	4.08±0.15	3.16±0.14
	18	8.04±0.12	7.79±0.13	6.79±0.14	5.78±0.13	4.60±0.13
	24	9.73±0.13	9.46±0.15	8.39±0.12	7.30±0.14	5.89±0.15
	30	11.17±0.13	10.89±0.14	9.73±0.13	8.62±0.11	7.11±0.19
4	6	5.18±0.01	4.39±0.02	2.98±0.01	1.70±0.01	0.84±0.01
	12	7.32±0.03	6.47±0.02	4.83±0.02	3.12±0.01	1.80±0.01
	18	8.54±0.03	7.67±0.02	5.98±0.02	4.10±0.01	2.55±0.01
	24	9.29±0.03	8.41±0.03	6.71±0.02	4.77±0.02	3.10±0.01
	30	9.78±0.04	8.92±0.03	7.20±0.03	5.22±0.01	3.49±0.02
39	6	3.77±0.03	0.80±0.03	0.17±0.03	0.06±0.03	0.01±0.03
	12	4.03±0.01	1.01±0.02	0.30±0.02	0.16±0.02	0.06±0.03
	18	4.14±0.00	1.11±0.01	0.37±0.01	0.21±0.01	0.09±0.01
	24	4.22±0.00	1.17±0.01	0.41±0.01	0.25±0.01	0.12±0.01
	30	4.27±0.00	1.20±0.00	0.43±0.00	0.27±0.00	0.13±0.00

TABLE 2. Experimental temperature coefficient $\Delta T/\Delta F$ [$\mathrm{K \cdot m^2/W}$] as a function of frequency (GHz), depth (mm) and exposure time (min) for gel. The fitting between the temperature (T) and incident power density (F) was performed over the linear range as $P < 2$W (1.9 GHz), $P < 0.5$W (4 GHz) and $P < 0.125$W (29 and 39 GHz). The results show mean ± standard deviation.

		Gel - $\Delta T/\Delta F$ [$\mathrm{K \cdot m^2/W}$] × 10^{-3}				
f (GHz)	t (min)	1 mm	6 mm	11 mm	16 mm	21 mm
1.9	6	3.60±0.01	3.45±0.01	2.77±0.02	1.99±0.03	1.37±0.02
	12	6.34±0.05	6.12±0.06	5.18±0.05	3.93±0.04	2.91±0.05
	18	8.52±0.13	8.32±0.13	7.20±0.10	5.69±0.04	4.30±0.07
	24	10.28±0.13	10.15±0.24	8.94±0.19	7.30±0.15	5.72±0.18
	30	11.48±0.07	11.35±0.24	10.21±0.23	8.64±0.24	6.95±0.28
4	6	6.18±0.12	4.74±0.05	2.71±0.01	1.23±0.03	0.48±0.01
	12	8.78±0.17	7.23±0.06	4.74±0.02	2.57±0.04	1.25±0.04
	18	10.17±0.18	8.59±0.08	6.03±0.04	3.58±0.06	1.94±0.06
	24	11.03±0.21	9.48±0.09	6.87±0.08	4.28±0.08	2.49±0.08
	30	11.68±0.21	10.14±0.12	7.46±0.08	4.77±0.08	2.90±0.09
29	6	3.14±0.06	0.87±0.02	0.26±0.01	0.06±0.00	0.00±0.00
	12	3.44±0.08	1.13±0.04	0.45±0.02	0.16±0.01	0.05±0.00
	18	3.60±0.10	1.26±0.04	0.55±0.02	0.23±0.01	0.08±0.00
	24	3.73±0.15	1.36±0.05	0.63±0.03	0.28±0.01	0.12±0.01
	30	3.92±0.19	1.46±0.07	0.70±0.04	0.32±0.02	0.15±0.01
39	6	3.35±0.04	0.91±0.02	0.25±0.01	0.05±0.00	0.01±0.00
	12	3.73±0.05	1.25±0.03	0.44±0.01	0.16±0.01	0.07±0.01
	18	3.95±0.07	1.45±0.05	0.55±0.01	0.23±0.01	0.12±0.01
	24	4.09±0.09	1.57±0.06	0.61±0.01	0.27±0.01	0.15±0.01
	30	4.13±0.11	1.62±0.07	0.64±0.01	0.29±0.01	0.16±0.01

As expected, the magnitude of the temperature rise in the tissue increases with increasing frequency, incident power and exposure time and closely follows a thermal diffusion model. What is less obvious, is that simply extrapolating the exposure time is a much less effective method of predicting the ultimate temperature rise in the tissue at the higher frequencies, as can be seen from Table 1. The temperature coefficient ($\Delta T/\Delta F$) increases with exposure time almost proportionally in the 4G band at 1.9 GHz, but more slowly in the 5G bands. For example, the $\Delta T/\Delta F$ ($\mathrm{K \cdot m^2/W}$) at 1 mm depth in the brain increases about 3.2 times at 1.9 GHz, about 1.9 times at 4 GHz and only about 1.1 times at 39 GHz

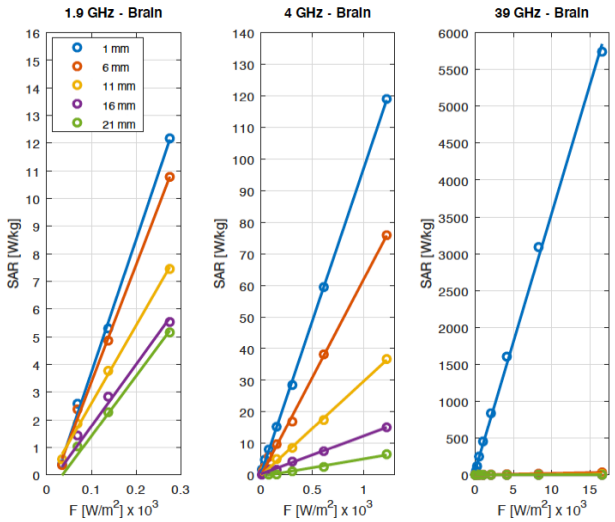

FIGURE 7. Experimental specific absorption rate (SAR) vs. incident power density (F) and depth (z) for brain at 1.9, 4 and 39 GHz.

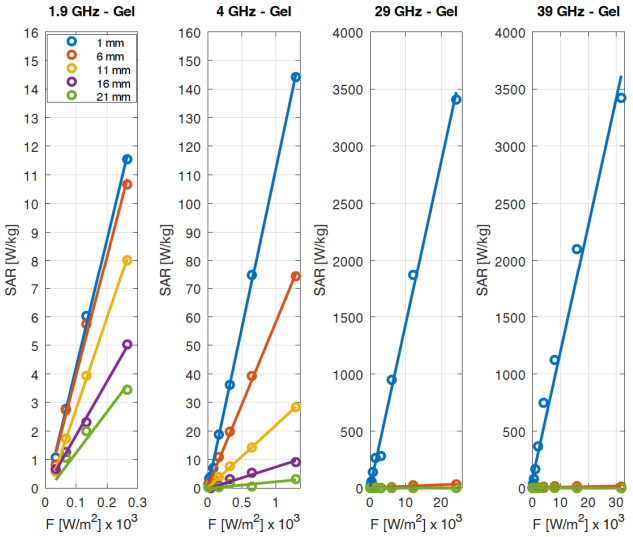

FIGURE 8. Experimental specific absorption rate (SAR) vs. incident power density (F) and depth (z) for gel at 1.9, 4, 29 and 39 GHz.

for increasing the exposures between 6 and 30 minutes. This also means that the surface temperature increases rapidly with higher frequency in the 5G bands and with the onset of heat diffusion has less dependence on exposure time.

Fitting the initial rise of temperature (T) versus time (t) for short periods ($t < 60$ s) for brain and gel in Figs. 2-4, we get a straight line with a slope of $\Delta T/\Delta t$ from which specific absorption rate (SAR) can be calculated as SAR$=C(\Delta T/\Delta t)$ for each frequency, depth and incident power density. Although, the specific heat (C), can be measured by MRI [50], [51], an average value of 3630 J/kg·K from the literature was used for the brain tissue [74]. Further, by plotting the SAR vs. F, we get a straight line with a slope of Δ(SAR)/ΔF for each frequency and depth as shown in Figs. 7 and 8. It is important to note that SAR measurements here are confined to the tips of the thermocouple wires and they may be considered as point SAR (pSAR) without averaging over a prescribed volume. Once high resolution pSAR is measured, it is easy to average over multiple thermocouple locations and a desired volume.

It is also important to see that the beam penetration, and therefore SAR, decreases with increasing depth at a frequency as shown in Figs. 7 and 8. Since SAR is measured over short times, the effects of thermal diffusion are not so apparent at higher depths and frequencies in Figs. 7 and 8, whereas ΔT is measured over long times, and the effects of thermal diffusion are apparent in Figs. 2 to 6. Deriving SAR by our thermal method at lower depths is sensitive to the time constant used due to the thermal diffusion.

Although SAR can be measured over very short times at high power density, the accuracy of fitting the $\Delta T/\Delta t$ decreases at lower power density and frequency. For fitting the SAR to the broad range of power density and frequency, we fitted ΔT vs. Δt from 10 s to 60 s with 10 s increments and found the optimum fitting times (Δt) of 40 s, 30 s and 20 s for the brain tissue at 1.9, 4 and 39 GHz, respectively. Using the data in Figs. 7 and 8, we derive incident power density dependent SAR coefficients, Δ(SAR)/ΔF (m^2/kg), as a function of frequency and depth for the brain and gel as shown in Tables 3 and 4, respectively.

TABLE 3. Experimental SAR coefficient Δ(SAR)/ΔF [m^2/kg] as a function of frequency (GHz) and depth (mm) for brain. The fitting between the temperature (T) and time (t) was performed over the linear range as $t < 40$ s (1.9 GHz), $t < 30$ s (4 GHz) and $t < 20$ s (39 GHz). The results show mean ± standard deviation.

	Brain - Δ(SAR)/ΔF [m^2/kg] × 10^{-2}				
f (GHz)	1 mm	6 mm	11 mm	16 mm	21 mm
1.9	4.80±0.18	4.23±0.16	2.81±0.10	2.23±0.24	2.17±0.16
4	9.70±0.06	6.23±0.09	3.00±0.05	1.21±0.03	0.56±0.02
39	34.90±0.49	0.20±0.01	0.06±0.01	0.00±0.00	0.00±0.00

TABLE 4. Experimental SAR coefficient Δ(SAR)/ΔF [m^2/kg] as a function of frequency (GHz) and depth (mm) for gel. The fitting between the temperature (T) and time (t) was performed over the linear range as $t < 50$ s (1.9 GHz) and $t < 30$ s (4, 29 and 39 GHz). The results show mean ± standard deviation.

	Gel - Δ(SAR)/ΔF [m^2/kg] × 10^{-2}				
f (GHz)	1 mm	6 mm	11 mm	16 mm	21 mm
1.9	4.47±0.15	4.15±0.24	3.19±0.06	1.88±0.08	1.43±0.24
4	11.25±0.12	5.80±0.10	2.20±0.04	0.76±0.05	0.23±0.06
29	14.25±0.35	0.14±0.01	0.00±0.00	0.00±0.00	0.00±0.00
39	11.12±0.46	0.05±0.02	0.00±0.00	0.00±0.00	0.00±0.00

Tables 3 and 4 show that SAR is similar at 1.9 and 4 GHz for the brain and gel but deviates significantly at 39 GHz. This is further confirmed with the FDTD analysis in the Appendix.

One of the notable conclusions of this study is the distinct difference in the behavior of the bovine brain tissue and the gel, indicating that the use of such substances in modelling RF effects must be re-evaluated, or at least more

carefully applied. The gel has a very narrow linear range of absorbed power versus temperature change compared to the brain tissue. The gel also undergoes a thermal transition where molecular motion and convection alter the thermal gradients and change the profile of the temperature versus time curves at higher frequency, power and exposure times. The use of gel over liquids is preferred to simulate lower convection rates in actual tissues, but in fact we observed that the gel still suffers from thermal convection under moderate heating with the millimeter waves. Therefore, the use of gel (or liquid) substances leads to a gross underestimation of the thermal gradients, and yields a temperature rise that is much smaller than that observed in the actual tissue. Differences observed between the brain tissue and gel, especially at the higher power levels and higher 5G frequencies, indicate that care must be taken when extrapolating tissue data from such measurements in addition to any differences in dielectric properties. A nonlinear relation between the temperature and power density indicates severe heating with subsequent tissue or gel damage, and the onset of thermal convection (gel state change).

These linear models provide temperature coefficients that can be used to generally determine and predict the amount of heating in the ex vivo brain or gel versus the depth, given the frequency, incident power density and exposure time. It is possible to use this data in the linear range specified to accurately predict the ΔT and SAR at any exposure time and depth at each of the recorded frequencies. Given the absence of any observed or reported resonances in the absorption coefficients, it is also possible to extrapolate the temperature data to any other frequency within the 5G band allocation when adjustments are made for the measured absorption coefficient and refractive index at frequency.

Since the 1 mm depth presents the worst-case exposure scenario and results in hot spots at the higher frequencies measured, and there is no evidence for resonances in other tissue types, these tables can be used to roughly predict the skin temperature rise given the frequency, incident power density and exposure time, once we have scaled for reflectivity and absorption coefficient differences. Reported real-time measurements on a monkey head [22] show that perfusion contributes relatively modest changes to overall heating deep within the tissue. Direct measurements on skin to verify this analogy are planned for the near future.

The 5G data transmission protocols will use both continuous wave (CW) and pulsed power, and these will have different impacts on the biological tissues. As a consequence, we tested pulse power effects on heating in our two samples at 1.9, 4 and 39 GHz. Pulsing the RF also gives us additional information on the thermal constants of the brain tissue and gel and allows us to readily measure sensitivity limits for the embedded thermocouples. We examined long pulse behavior (1 s to 30 s single pulse), and 50% duty cycle short pulses (1 μs, 1 ms and 1 s) for 30 minutes duration.

In the first set of pulsed experiments, we examined long duration exposures with varying pulse lengths and a fixed

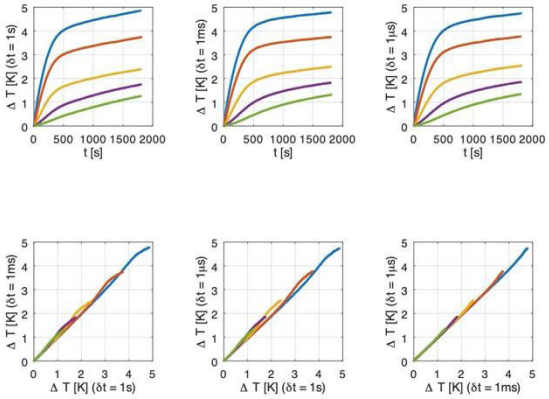

FIGURE 9. Experimental temperature rise (ΔT) vs. time (t), depth (Δz) and pulse length (δt) for gel at 4 GHz. The top row (from left to right) shows pulse lengths of 1 s, 1 ms and 1 μs with a duty cycle of 50%. The bottom row (from left to right) are plots comparing different pulse lengths against one another to confirm that the behavior at all pulse lengths is consistent and linear. Line colors refer to depths of 1, 6, 11, 16 and 21 mm, respectively.

pulse duty cycle of 50%. We performed this series of measurements only on the gel in order to test the theory. The experimental temperature rise (ΔT) vs. time (t) and pulse length (δt) using equal duty cycle (on/off times = 1:1) and a pulse power of 2 W for the gel at 4 GHz are shown in Fig. 9 for the five different thermocouple positions within the sample. The top row (from left to right) shows the temperature rise versus time (up to 30 minutes) for pulse lengths of 1 s, 1 ms and 1 μs at 2 W with a duty cycle of 50%, and the bottom row (from left to right) plots the temperature changes from the various pulse widths against each other to show that the thermal effects are all responding similarly. The slope of plots would be equal to 1 ($y = x$) if the results from both sets were perfectly identical. The measured heating in the sample at 2 W exposure over 30 minutes for the 50% duty cycle pulses was equal to the heating observed at 1 W with a CW signal, simply confirming that the impact of the pulses is linear with duty cycle over the periods we examined.

In a second series of pulse measurements, to visualize transient effects on both bovine brain and gel, we used a single pulse of varying duration and fixed power level (2 W at 1.9 and 4 GHz and 1 W at 39 GHz - since 2 W at this frequency damaged the tissue) and measured the temperature response at different depths in the samples at 1.9, 4 and 39 GHz. A compilation of all the measurements is shown in Fig. 10.

Fig. 10 shows that the brain and gel samples respond similarly to the pulsed power at 1.9 and 39 GHz, but there is a difference in temperature rise between the two samples at 4 GHz. This is attributed to differences in the dielectric absorption coefficient of the brain and gel at this frequency (see Appendix, Fig. 11). Note that the 39 GHz plots show the extreme power concentration near the surface of the samples and the embedded thermocouples show the profiles expected

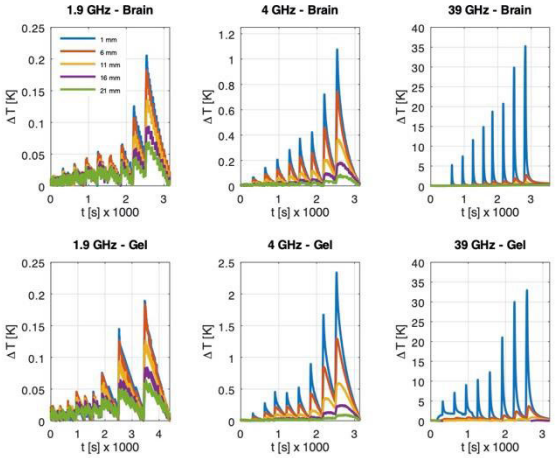

FIGURE 10. Application of single pulses with varying lengths (1, 2, 3, 4, 5, 10, 20 and 30 s) at 2 W power levels for 1.9 and 4 GHz, and 1 W power level for 39 GHz. Brain tissue (top row) and gel (bottom row), at 1.9, 4 and 39 GHz.

from a thermal diffusion model with a temperature rise that tracks the changes in total incident power.

The method employed in this study uses individual thermocouples to record the temperature in the tissue at specific predetermined depths along a single axial pathway. In our prior study at 1.9 GHz, we employed an MRI, which has the advantage of recording the volume temperature rise at any point in the tissue. However, MRI has several disadvantages [47]. First, it has magnet compatibility issues that need to be resolved to accommodate the well calibrated waveguide injection system we used in this study. Second, the high field MRI's intense RF pulses at 400 MHz give rise to significant heating in addition to the incident RF power studied here [75]–[77]. Third, there is a high cost to reserving the long uninterrupted scanner time required for these lengthy experiments (more than 12 hours continuously per frequency and sample). In contrast, our embedded thermocouple technique has a temperature accuracy of better than 0.1°C, temporal resolution of 1 s, and a spatial resolution of 1 mm and has been shown to be sensitive enough to record changes in temperature due to an incident power level of 1 mW in the millimeter wave bands (29 and 39 GHz) in a 6-minute exposure.

The spatiotemporal variation of temperature in the tissue can be approximated by the modified Pennes' bioheat equation including the thermal convection terms [78]:

$$\frac{\partial T}{\partial t} = D\nabla^2 T - wk\,(T - T_a) + \frac{Q}{\rho C} - \frac{hA}{\rho C V}\,(T - T_\infty) \qquad (1)$$

where $D = \kappa/\rho C$ is thermal diffusivity (m^2/s), κ is thermal conductivity (W/m $\cdot$ K), ρ is density (kg/m^3), C is specific heat of tissue (J/kg$\cdot$K), $Q = P_a/V$ is absorbed power density (W/m^3), P_a is absorbed power (W), w is perfusion rate (1/s), k is the ratio of ρC for blood to tissue, T_a is the arterial temperature (K), T_∞ is the ambient temperature (K), h is heat transfer coefficient (W/m^2 $\cdot$ K), A is surface area (m^2) and V is volume (m^3).

Given the absence of perfusion in ex vivo tissue and the accurate values for the specific heat, density, thermal diffusivity, heat transfer coefficient, and absorbed power density at the boundary, Eq. (1) makes it possible to derive the temporal and spatial variations of temperature in the tissue and compare these to the measurements shown in Figs 2-4. In our prior MRI studies, we were able to measure the thermal diffusivity (D), thermal conductivity (κ) and specific heat (C) of a gel [50], [51], [70].

The semi-infinite modeling solution of Eq. (1) with a constant flux boundary condition without the perfusion and convection terms, results in [51], [79].

$$T(z,t) = T_\infty + \frac{F_0}{\kappa}\left[2\sqrt{\frac{Dt}{\pi}}\exp\left(-\frac{z^2}{4Dt}\right) - z\left(1 - \mathrm{erf}\frac{z}{2\sqrt{Dt}}\right)\right] \qquad (2)$$

for one dimensional heat diffusion along the z direction and

$$\Delta T(z,t) = \frac{F_0}{\kappa}\left[\frac{d}{\sqrt{\pi}}\exp\left(-\frac{z^2}{d^2}\right) - z\cdot\mathrm{erfc}\left(\frac{z}{d}\right)\right] \qquad (3)$$

where $\Delta T(z,t) = T(z,t) - T_\infty$, T_∞ is initial temperature, $F_0 = P_0/A$ is the surface power density or flux in x-y plane at $z = 0$, P_0 is the surface power, A is the surface area, κ is the thermal conductivity, $d = 2\sqrt{Dt}$ is the root mean square diffusion length, D is the thermal diffusivity, erf is the error function and erfc is the complementary error function. Fitting the measured ΔT data numerically to Eq. (3) and plotting the $d = 2\sqrt{Dt}$ vs. $\sqrt{t}$ yields a straight line with a slope of $2\sqrt{D}$ and the thermal diffusivity coefficient (D) for the substance [51]. This thermal method is highly accurate and reproducible as previously shown with a high-resolution MRI [51].

A preliminary analysis shows that the measured data at 4 GHz can approximately satisfy the thermal model in Eq. (3). Using the experimental ΔT data at 4 GHz and Eq. (3), we measured a thermal diffusivity of $1.23 \cdot 10^{-7}$ m^2/s for the ex vivo bovine brain tissue vs. $1.28 \cdot 10^{-7}$ m^2/s calculated from $D = \kappa/\rho C$ with $\kappa = 0.51$ W/m $\cdot$ K, $\rho = 1100$ kg/m^3 and $C = 3630$ J/kg $\cdot$ K for brain tissue in the literature.

At 4 GHz, the beam penetration and absorption appear optimized providing a constant heat flux boundary condition as shown to be consistent with the thermal model in Eq. (3). The diffusivity estimates start to deviate from the expected value at 1.9 GHz due to much higher beam penetration, and at 39 GHz due to severe beam concentration and absorption at the surface. At our current low spatial resolution of $\Delta z = 5$ mm and maximum depth of $z = 21$ mm, using only three spatial points away from the surface (11 to 21 mm), we measure a thermal diffusivity of $1.38 \cdot 10^{-7}$ m^2/s and $0.81 \cdot 10^{-7}$ m^2/s for brain tissue at 1.9 and 39 GHz, respectively. At the depth of $z = 1/\alpha$, the power density drops to about 1/3 of its value at $z = 0$. Analyzing the data from our previous study using an MRI and a 1.9 GHz $\lambda/2$ dipole antenna RF injection source [47], we measured a thermal diffusivity of $1.34 \cdot 10^{-7}$ m^2/s for brain tissue which is

close to the value obtained using the 1.9 GHz waveguide injection source in this study. However, the RF waveguide setup at 4 GHz is sufficient to measure the thermal diffusivity of ex vivo brain tissue fairly accurately. These results are preliminary and we are currently working on extending these thermal models to a broader range of frequencies using the high-resolution MRI and three-dimensional temperature data.

Under RF exposure, the specific absorption rate, SAR $= P_a/\rho V$. In very short exposures and in the absence of perfusion, thermal conduction and convection, SAR can be computed by the thermal method as SAR $= C(dT/dt)$ in contrast to the field probe method, where SAR $= \sigma|E|^2/\rho$, σ is the electrical conductivity of the tissue (S/m) and E is the root mean square electric field strength of the tissue (V/m).

The recent IEEE C95.1 standard sets dosimetric reference limits (DRL) and exposure reference levels (ERL) expressed in terms of in-situ and external limits, and ICNIRP guidelines use basic restrictions and reference levels [39], [40]. Both IEEE and ICNIRP use the same safety limits and levels for the exposure of persons in unrestricted and restricted environments (public/occupational). The occupational limits are 5 times higher than the public limits. It is useful to look in detail at these limits and exposure times as they relate and apply to the measurements presented in this paper.

The new DRLs use SAR below 6 GHz and epithelial power density (IEEE) or absorbed power density (ICNIRP) above 6 GHz for persons in unrestricted and restricted environments (public/occupational) as given in Table 5. The SAR is averaged over 6 min for local exposure and over 30 min for whole-body exposure. The SAR for local exposure is averaged over 10 g of tissue in a volume in the shape of a cube. The absorbed (epithelial) power density (PD) for local exposure is averaged over 6 min and 4 cm^2 or 1 cm^2 (>30 GHz) of body surface area in the shape of a square.

TABLE 5. DRLs for exposures of persons in unrestricted and restricted environments (public/occupational).

Exposure Conditions	$f < 6$ GHz	$f > 6$ GHz
SAR (W/kg) – Whole Body [a]	0.08 / 0.4	
SAR (W/kg) – Head / Torso [b]	2 / 10	
SAR (W/kg) – Limb [b]	4 / 20	
PD (W/m^2) [c]		20 / 100

[a] Averaged over 30 min.
[b] Averaged over 6 min and 10 g cubic mass.
[c] Averaged over 4 cm^2 or 1 cm^2 (> 30 GHz), epithelial power density is allowed to exceed the DRL values by a factor of 2, with an averaging area of 1 cm^2.

The SAR is measurable below 6 GHz by the field probe method but not above 6 GHz due to the decreased beam penetration and increased power absorption near the surface of the tissue requiring the measurement of epithelial (absorbed) power density. The local SAR limits for cell phones (<6 GHz) have been set by the FCC in the USA as 1.6 W/kg averaged over 1 g mass and by the EC in the EU as 2.0 W/kg averaged over 10 g mass against peak exposures [11], [80].

TABLE 6. ERLs for local exposures of persons in unrestricted and restricted environments (public/occupational).

f (GHz)	Formula / Range [c]	PD (W/m^2) [d]
1.9 GHz [a]	$1.19 \times f_M^{0.463}$	39.23 / 196.15
4 GHz [b]	$2 < f_G < 6$	40 / 200
39 GHz	$55 \times f_G^{-0.177}$	28.76 / 143.8

[a] f_M is the frequency in MHz.
[b] Limits in the range, f_G is the frequency in GHz.
[c] Public limits, multiplied by 5 for occupational limits.
[d] Averaged over 6 min, 4 cm^2 or 1 cm^2 (> 30 GHz), epithelial power density is allowed to exceed the DRL values by a factor of 2, with an averaging area of 1 cm^2.

TABLE 7. ERLs for whole-body exposures of persons in unrestricted and restricted environments (public/occupational).

f (GHz)	Formula / Range [c]	PD (W/m^2) [d]
1.9 GHz [a]	f_M / 200	9.5 / 47.5
4 GHz [b]	$2 < f_G < 300$	10 / 50
39 GHz	$2 < f_G < 300$	10 / 50

[a] f_M is the frequency in MHz.
[b] Limits in the range, f_G is the frequency in GHz.
[c] Public limits, multiplied by 5 for occupational limits.
[d] Averaged over 30 min.

TABLE 8. EDs for local exposures of persons in unrestricted and restricted environments (public/occupational) for $0 < t < 6$ min.

f (GHz)	ED (kJ/m^2) [d]
1.9 GHz [a]	$0.058 f_M^{0.86} \times 0.36\ [0.05 + 0.95\ (t/360)^{0.5}]$
4 GHz [b]	$40 \times 0.36\ [0.05 + 0.95\ (t/360)^{0.5}]$
39 GHz [c]	$55/f_G^{0.177} \times 0.36\ [0.05 + 0.95\ (t/360)^{0.5}]$

[a] f_M is the frequency in MHz, t is the time in min.
[b] Limits in the range, $2 < f_G < 6$ GHz.
[c] f_G is the frequency in GHz.
[d] Public limits, multiplied by 5 for occupational limits.

The ERLs for local exposure of persons in unrestricted and restricted environments (public/occupational) are given in Table 6 for 1.9, 4 and 39 GHz, respectively. The incident PD for local exposure is averaged over 6 min, 4 cm^2 or 1 cm^2 (>30 GHz) body surface area in the shape of a square.

The ERLs for whole-body exposure of persons in unrestricted and restricted environments (public/occupational) are given in Table 7 for 1.9, 4 and 39 GHz, respectively. The incident PD for whole-body exposure is averaged over 30 min.

The incident energy density (ED) levels, integrated over time interval, $0 < t < 6$ min, for local exposure of persons in unrestricted and restricted environments (public/occupational) are given in Table 8 for 1.9, 4 and 39 GHz, respectively.

The local exposure of persons in unrestricted and restricted environments (public/occupational) to pulse trains or single intense pulses is given in Table 9. For intense pulses in the millimeter-wave frequency range (>30 GHz), the maximum local incident ED per pulse (averaged over 1 cm^2) is limited to $<0.2\ \delta^{0.5}$ kJ/m^2 and $<\delta^{0.5}$ kJ/m^2 for persons in unrestricted and restricted environments, respectively. The pulse width (δ) is in seconds.

TABLE 9. EDs for local exposures of persons in unrestricted and restricted environments (public/occupational) to pulse trains. The public limits below are multiplied by 5 for occupational limits.

ED (J/kg) < 6 GHz [a]	ED (J/m^2) > 6 GHz [b]
$\sum_{i=1}^{n} (\mathrm{pSAR_i} \times \delta_i) \leq \frac{\mathrm{DRL} \times t_a}{5}$	$\sum_{i=1}^{n} (\mathrm{pPD_i} \times \delta_i) \leq \frac{\mathrm{ERL} \times t_a}{5}$

[a] $\mathrm{pSAR_i}$ is peak SAR, δ_i is pulse width (s) of ith pulse in any period of 100 ms, t_a is 6 min averaging time.
[b] $\mathrm{pPD_i}$ is peak PD.

Using the IEEE safety limits and the experimental data in Table 1, it is possible to predict the temperature rise in the brain tissue at a given frequency, depth and exposure time. For example, using the ERLs (ΔF) of 39.23, 40 and 28.76 W/m^2 in Table 6 for local exposures of persons in an unrestricted environment (public), and the $\Delta T/\Delta F$ values of 3.51, 5.18 and 3.77 $\times$ 10^{-3} K $\cdot$ m^2/W for 6 min exposure at 1 mm depth from Table 1, we calculate a temperature rise, $\Delta T = (\Delta T/\Delta F)\Delta F$, of 0.14, 0.21 and 0.11°C in brain tissue at 1.9, 4 and 39 GHz, respectively. The temperature rise for local exposures of persons in a restricted environment (occupational) are five times higher at 0.70, 1.05 and 0.55°C, respectively.

Similarly, using the ERLs for local exposure of the public in Table 6 and Δ(SAR)/ΔF values in Table 3, we can estimate the SAR = $(\Delta(\mathrm{SAR})/\Delta F)\Delta F$ as 1.8, 3.9 and 10 W/kg in brain tissue at 1 mm depth at 1.9, 4 and 39 GHz, respectively. As stated earlier, the tip of the fine gauge thermocouple wire is confined to a very small volume in the tissue, so the SAR measurements here correspond to the point SAR (pSAR). The SAR values decrease with distance and more drastically with frequency as seen in Figs. 7 and 8, and Tables 3 and 4. Assuming an average surface power density in the x-y plane decreasing in the z direction along the thermocouple locations, pSAR may be spatially averaged over $z = 10$ mm distance or over three thermocouple locations (each 5 mm apart) to measure the SAR averaged over 1 cm^3 or 1 g of tissue as per FCC guidelines. Averaging over 1 mm to 11 mm depths in Table 3 and using the ERLs in Table 6, we calculate the SAR averaged over 1 g of brain tissue as 1.5, 2.5 and 3.4 W/kg at 1.9, 4 and 39 GHz, respectively.

It should be noted that the frequency (and wavelength), waveguide aperture area or dipole antenna length, and average power density are all interrelated. Increasing frequency, decreases the appropriate waveguide area or the resonant antenna length and increases the average incident power density drastically for any prescribed power. Using 1 W of incident power in each of the waveguide sources at 1.9, 4 and 39 GHz, results in the average incident power density of 138, 613 and 16,578 W/m^2 respectively at the tissue surface, and raises the temperature of the bovine brain tissue at 1 mm depth by 0.5, 3 and 62°C with only a 6 minute exposure time. This fact needs to be carefully considered when specifying incident power requirements for low and high frequency RF sources. The power density safety limits in Table 6 for our waveguide sources at 1.9, 4 and 39 GHz, correspond to incident power levels of 285, 65 and 1.7 mW for public, and 1425, 325 and 8.5 mW for occupational exposures, respectively. Although the range of incident power levels used in this study exceeds the IEEE C95.1 safety limits, this broad range is necessary for determining the $\Delta T/\Delta F$ and Δ(SAR)/ΔF coefficients over a wide range of parameters. We are not suggesting that these levels are intentionally present in either the public or occupational exposures allowed under current safety standard and guidelines.

As can be seen from Tables 5 to 9, current safety limits are fairly complicated, and depend on the frequency, exposure type and time. The thermal method presented here is capable of measuring both temperature change (ΔT) and specific absorption rate (SAR), and is applicable to a broad range of frequency and exposures, above and below the 6 GHz demarcation zone recommended in IEEE C95.1 standard. The thermal method is complicated by the combined effects of beam penetration, absorption and thermal diffusion, but by careful analysis it provides both the transient temperature history and specific absorption rate that are necessary for assessing safety levels in terms of the magnitude of the temperature rise over a given exposure time. We demonstrate that the ultimate effect can be assessed with absolute temperature rise in the tissue at prescribed incident power density, frequency and depth, which is a better measure of the radiation absorption effects and safety in humans.

V. LIMITATIONS OF THE STUDY

In this study, we use RF waveguide sources directly irradiating ex vivo bovine brain inside plastic containers to quantify the temperature rise and the specific absorption rate in the brain tissue as a function of frequency, incident power density and depth. However, this study does not take into account the layers of skin, fat, muscle and skull containing the brain in a realistic head model. The actual power density and the heat diffusion reaching the surface of the brain in a real head will obviously not be the same as the values we show in this study, where our power is incident directly on the brain tissue. However, the derived thermal coefficients and linear behavior are properties of the tissue and can be used to predict temperature changes as a function of incident RF power density. In addition, the behavior of skin, fat, muscle and bone can be roughly extrapolated within the same incident power regimes given a priori measurements of the dielectric and thermal diffusion constants. It is also interesting to note that the current safety limits of 28.76 and 143.8 W/m^2 (public and occupational) applied to our directional RF waveguide source at 39 GHz would correspond to only 1.7 and 8.5 mW incident power levels, which is an extremely limited amount of power availability for a broad distribution communications system.

The accurate measurement of SAR by thermal methods such as ours near the surface and at low power density can be affected by the thermal diffusion time, and extra care must

be taken. The diffusion length, $d = 2\sqrt{Dt}$, must be shorter than the depth ($d < z$) at which the SAR is being measured. This requires exposure to the radiation over a fairly short time for characterizing shallower depths (for example, $t < 2$ s for $d < 1$ mm) during the initial temperature rise and for fitting the $\Delta T/\Delta t$ and SAR $= C(\Delta T/\Delta t)$. Although, short time exposures can easily be used for higher power densities and at higher frequencies, the accuracy of fitting the $\Delta T/\Delta t$ decreases at lower power density and frequency. For purposes of covering the greatest power density range in our bovine brain tissue, we used fitting times that yielded a highly linear slope of $\Delta T/\Delta t$. Using Δt of 40, 30 and 20 s for 1.9, 4 and 39 GHz respectively, and the thermal diffusion coefficient of $D = 1.23 \cdot 10^{-7}$ m^2/s as measured in this study, we calculated the diffusion length (d) as 4.4, 3.8 and 3.1 mm in brain tissue. This shows that SAR measurements at depths from 6 to 21 mm are free of thermal diffusion effects, whereas SAR measurements at 1 mm depth are somewhat affected by thermal diffusion over these fitting times.

VI. SUMMARY

In this paper, we present for the first time, a simple, highly accurate test system for measuring the temperature rise and the specific absorption rate in tissue samples and liquid or gel simulants as a function of frequency, RF exposure power and time – pulsed and CW. We use this setup to make, and compare, carefully calibrated measurements of bovine brain tissue and a gel simulant, Triton X and water, at both 4G (1.9 GHz) and newly allocated 5G frequency bands (4 GHz - 39 GHz). We show the effects of beam concentration, focusing, absorption and heat diffusion at all three frequencies and delineate a linear range over which we can derive highly accurate coefficients ($\Delta T/\Delta F$ and Δ(SAR)$/\Delta F$) that can be used to predict the temperature rise and the specific absorption rate at prescribed depths and exposure times within the tissue or gel at power levels that go down to detectable limits (<1 mW). This method may be used to evaluate a wide range of RF radiation sources, tissues and simulants.

We also note that the impact of relatively modest incident RF power (1 W) and short exposure times (6 minutes CW and 30 second pulsed) at 39 GHz using a single mode waveguide source for the exposure, results in extremely large power density (16.5 kW/m^2) and temperature rise (>60°C for CW, >35°C for 30 s pulse) in both bovine brain tissue and gel. This same temperature rise can be expected on skin (which has very similar dielectric properties) when such large surface power densities are present in very close proximity to the RF source or antenna, perhaps emanating from millimeter-wave base stations, handsets, or wireless-enabled appliances or kiosks. Although, current safety limits of 28.76 and 143.8 W/m^2 for power density in unrestricted (public) and restricted (occupational) environments, respectively should prevent such exposures, the resulting limits on RF power generation of only 1.7 to 8.5 mW from a directional RF source, such as our waveguide at 39 GHz, in the vicinity, will greatly limit the application potential for any such communications system.

In the USA, the FCC and FDA are overseeing the implementation of millimeter wave technology in the public realm and more studies are needed to help guide the science, technology and policy. Our experimental method can provide threshold temperature and SAR values for both occupational and public exposures to millimeter waves with surface power densities from 16.5 W/m^2 to 16.5 kW/m^2 and exposure times from 1 second to 30 minutes.

Finally, we use our new data and this RF method to derive a thermal diffusivity coefficient for the ex vivo bovine brain tissue that is consistent with our prior measurements using an MRI. This is the first time that the thermal diffusivity of ex vivo bovine brain tissue has been directly measured by this thermal RF method [47], [50], [51], [70].

APPENDIX
MEASURED AND DERIVED DIELECTRIC PARAMETERS FOR SAMPLES

Since the frequency range of 5G covers a region of the electromagnetic spectrum wherein the complex index of refraction of water, and hence water-based tissue, varies considerably, it is instructive to examine the impact of the tissue on the RF beam properties. The real part of the refractive index will cause significant reflection and refraction as the microwave power impinges on the tissue, and the resulting absorption versus surface area and depth will depend strongly on the electromagnetic field distribution.

In order to get a direct measure of our tissue and gel properties across the 5G bands we employed a Keysight vector network analyzer (PNA E8363B) and specially supplied liquid immersion probe (Keysight 85070E) to record the real and imaginary parts of the dielectric constant for all the samples between 0.1 and 40 GHz. Fig. 11 shows the real and imaginary parts of the dielectric constant (ε' and ε'') for our Bovine brain samples (fresh and previously frozen and thawed), the Triton X gel and DI water (as a reference).

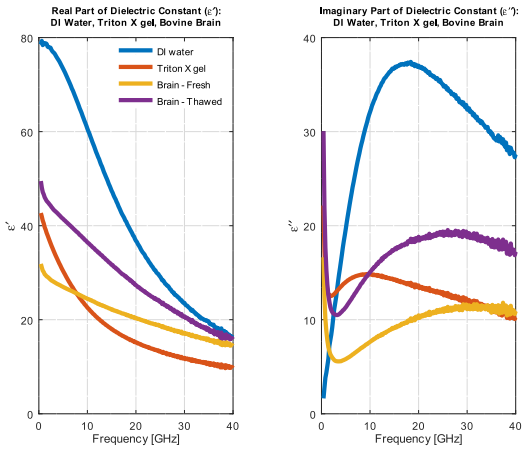

FIGURE 11. Keysight 85070E probe readings for ε' and ε'' vs. frequency from 0.1-40 GHz.

TABLE 10. Measured and derived dielectric parameters for bovine brain tissue and Triton X gel.

Frequency	1.9 GHz	4 GHz	29 GHz	39 GHz
Parameter	**BOVINE BRAIN**	**BOVINE BRAIN**	**BOVINE BRAIN**	**BOVINE BRAIN**
ε'	29.00	27.51	17.43	14.69
ε''	6.24	5.59	11.01	11.49
Index, n	5.42	5.27	4.36	4.08
Wavenumber, k	0.576	0.530	1.262	1.407
α (cm^{-1})	0.46	0.89	15.35	23.00
tan δ	0.215	0.203	0.632	0.782
σ (*Siemens/m*)	0.143	0.254	11.222	19.487
Power Reflection Coeff. Γ, normal.	0.47	0.46	0.39	0.37
Parameter	**TRITON X GEL**	**TRITON X GEL**	**TRITON X GEL**	**TRITON X GEL**
ε'	37.63	32.43	12.13	9.84
ε''	12.51	13.52	11.91	10.85
Index, n	6.22	5.81	3.82	3.50
Wavenumber, k	1.006	1.163	1.56	1.55
α (cm^{-1})	0.81	1.95	18.98	25.34
tan δ	0.33	0.42	0.98	1.10
σ (*Siemens/m*)	0.442	1.257	18.887	25.941
Power Reflection Coeff. Γ, normal.	0.52	0.50	.34	0.31

$$n = \sqrt{\frac{|\varepsilon|+\varepsilon'}{2}}, \text{ where } |\varepsilon| = \sqrt{(\varepsilon')^2 + (\varepsilon'')^2}. \; k = \sqrt{\frac{|\varepsilon|-\varepsilon'}{2}}. \; \alpha = \frac{4\pi f k}{c}. \; \tan\delta = \varepsilon''/\varepsilon'.$$

$$\sigma = 2\pi f \varepsilon_0 \varepsilon'' \cdot \tan\delta, \text{ where } \varepsilon_0 \text{ is the free space conductivity, and } \Gamma = \left|\frac{n-1}{n+1}\right|^2$$

Table 10 lists the measured values of the real and imaginary parts of the dielectric constant and the derived values of the refractive index, wavenumber, absorption coefficient, loss tangent, conductivity, and power reflection coefficient at the frequencies we have examined in this paper. Note that the brain tissue and gel may vary in dielectric properties from sample to sample. The measurements here were applied to the same samples used in our experiments.

We tested frozen-then-thawed bovine brain samples in order to determine whether there was any noticeable change in dielectric properties due to this method of tissue handling, since being able to store samples for longer periods of time is advantageous. As can be seen in the Fig. 11, however, there are significant changes both to the real and imaginary parts of the dielectric constant of the tissue when it is frozen and then warmed back up to room temperature for measurements. The refractive index and the loss tangent for the thawed brain tissue are both significantly higher than fresh tissue over the entire 4G and 5G frequency range, likely due to increased water content from the freeze-thaw process. For this reason, we did not use any of the frozen samples for our measurements and suggest that this technique is problematic for RF measurements on tissue in this frequency range.

We measured the reflection coefficients at 1.9, 4 and 39 GHz on the actual brain and gel samples in their plastic containers and through the exciting waveguides, using a vector network analyzer set to S11 before our measurements were started. We also checked these rough values against an FDTD calculation using the measured dielectric constant (real and imaginary) of the brain and gel as shown in Fig. 11. These values were compared with the Fresnel equations for a plane wave at normal incidence and found to be within a few percent. However, one of the primary reasons we are using this new thermal test system, rather than a field measurement method for determining *dT/dP* or *dT/dF* is so we do not have to know the actual absorbed power in the tissue. The reflection coefficient is already incorporated into the measurement of *dT/dP* or *dT/dF* and only the incident power is important. Although it is true that the reflection coefficient will change slightly as the tissue water content varies and as the tissue temperature changes, the *dT/dP* or *dT/dF* will be an accurate reflection of the real incident power effects. This is one of the strengths of our method.

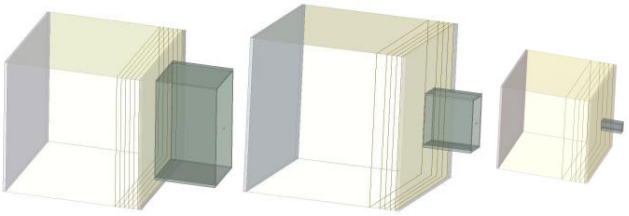

FIGURE 12. WR-430 waveguide with large cube (left), WR-187 waveguide with large cube (middle) and WR-28 waveguide with small cube (right) for 1.9, 4 and 39 GHz simulations. The cube dimensions are 150 × 150 × 150 mm and 96 × 96 × 96 mm, and the sketched planes are at 1, 6, 11, 16 and 26 mm, respectively.

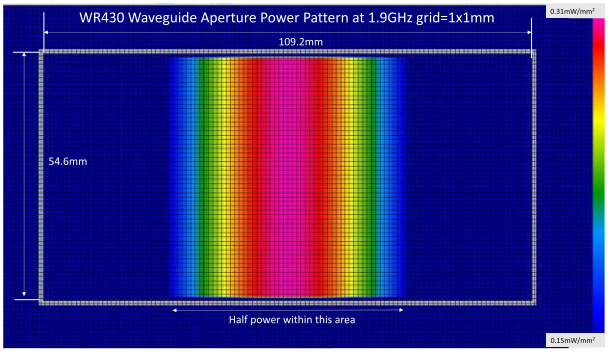

FIGURE 13. Power distribution at 1.9 GHz across the aperture of the WR-430 waveguide. 1 W incident.

ELECTROMAGNETIC ANALYSIS

Utilizing the values measured in section above for brain and gel samples, it is possible to construct a finite difference time domain (FDTD) analysis of the actual microwave signals as they exit the coax-to-waveguide transition and enter the sample container. We employed an FDTD simulator (Quickwave, QWED Ltd., Warsaw, Poland) that is particularly well suited for our test setup. The FDTD analysis setup is shown in Fig. 12 for the two sample containers and three waveguides we employed in the experiments. The calculated power patterns (linear scale) across the output aperture for the three waveguide injection systems we employed (WR-430, WR-187 and WR-28) are shown in Figs. 13, 14 and 15 with calibrated gridlines. A 39 GHz plot of the vertical and horizontal power in the WR-28 waveguide (cross sections through the central planes) shows the

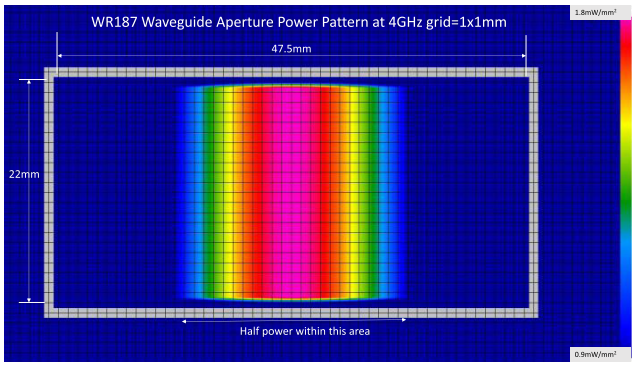

FIGURE 14. Power distribution at 4 GHz across the aperture of the WR-187 waveguide. 1 W incident.

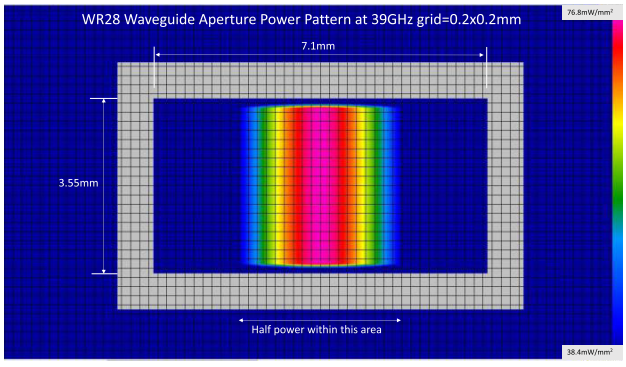

FIGURE 15. Power distribution at 39 GHz across the aperture of the WR-28 waveguide. 1 W incident.

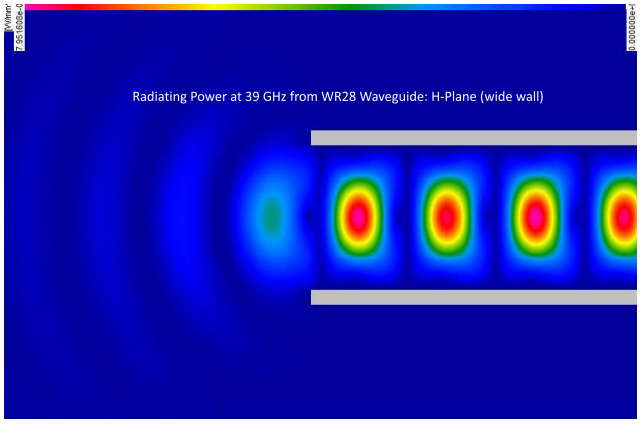

FIGURE 16. Power distribution in the WR-28 waveguide at 39 GHz looking down on the wide wall. Cross section at the center of the vertical wall.

propagating waveforms in Figs. 16 and 17. Note that these plots assume that the waveguide is open to free space with no sample and sample holder in place at the aperture.

When we add the plastic sample holder and tissue to the output port of the waveguide, we can get a picture of the power as it propagates through. Figs. 18, 19 and 20 show a series of power cross sections as we step through the sample holder and bovine brain at positions of 0, 1, 6, 11, 16 and 26 mm along the z direction. In all cases the color-coded

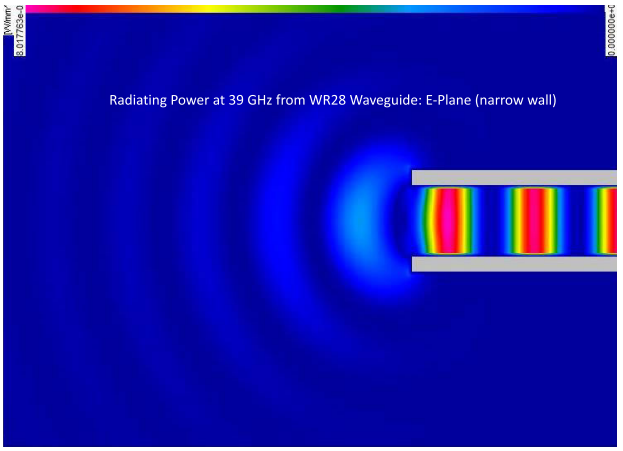

FIGURE 17. Power distribution in the WR-28 waveguide at 39 GHz looking down on the narrow wall. Cross section at the center of the horizontal wall.

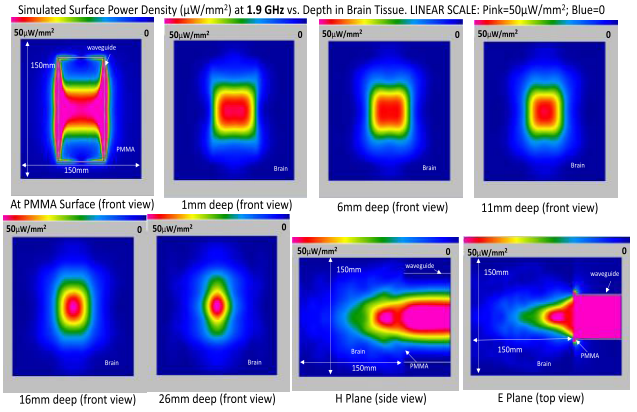

FIGURE 18. Simulated power vs depth in the bovine brain tissue at 1.9 GHz. Depths cover the range of thermocouple positions in the experiments. The last two plots at the lower right show the power propagating along the z-axis (into the sample) at the two principle planes that cross the center of the waveguide. All plots are to scale.

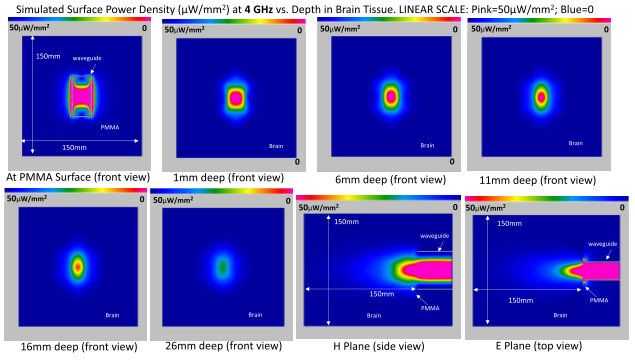

FIGURE 19. Simulated power vs depth in the bovine brain tissue at 4 GHz. Depths cover the range of thermocouple positions in the experiments. The last two plots at the lower right show the power propagating along the z-axis (into the sample) at the two principle planes that cross the center of the waveguide. All plots are to scale.

scales are linear and the incident power is 1 W. The two last views at the lower right of each figure show the E and H plane power at the central planes as the RF enters the tissue holder

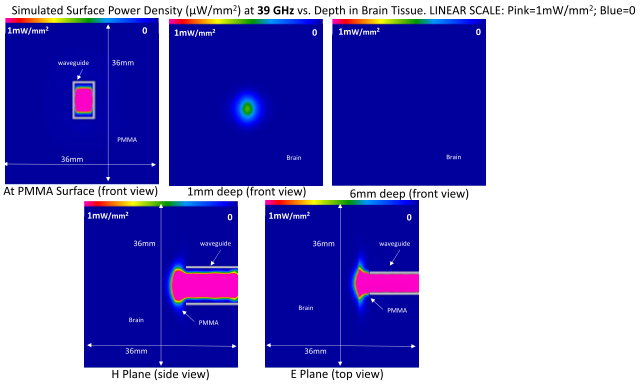

FIGURE 20. Simulated power vs depth in the bovine brain tissue at 39 GHz. Power is only visible out to 1 mm depth. The last two plots at the bottom show the power propagating along the z-axis (into the sample) at the two principle planes that cross the center of the waveguide. All plots are to scale.

and propagates through the tissue. There are several points to highlight in these simulations. First, looking at Fig. 18, the power entering the tissue is refracted and focused to an elliptical spot well inside the tissue. However, as the wave propagates, it is also absorbed by the highly conductive tissue. Hence all the power is dissipated well before we reach the end of the plastic container. At 4 GHz, the loss tangent is significantly higher than at 1.9 GHz and the penetration of the power is less and the roll-off with depth is greater. We also notice the reflection and spread of the power in the plastic (PMMA) wall of the container. At 39 GHz, the power falls off to nearly zero before we get to the second thermocouple depth at 6 mm. The two side views show that all the loss is concentrated near the surface of the brain tissue and there is little impact from focusing because the absorption coefficient, α, is so large at this frequency.

It is possible to estimate the average power density at the surface of the tissue using the simulated field and power patterns and the measured reflection coefficient of the tissue. We take the 10 dB power spot dimensions at a position just one or two FDTD cells below the surface of the simulated tissue (after the power has left the waveguide and passed through the PMMA container wall) and determine the area for 90% of the imposed power. The power patterns are more rectangular than circular within this close distance of the waveguide aperture for the 1.9 and 4 GHz waveguides, but the 39 GHz power pattern is more ellipsoidal after passing through the container wall. The areas measure as 5,933, 1,304 and 50 mm^2 respectively after closely examining power pattern plots similar to those shown in Figs. 18-20. Accounting for the measured reflection coefficients of 0.47, 0.46 and 0.37 at 1.9, 4 and 39 GHz (Table 10), which agree with the FDTD calculated values with the container present and using as an example, 1W of incident power, we derive an average power density of 138, 613 and 16,578 W/m^2 at the tissue surface for the waveguides.

Although the FDTD tool only gives an estimate of the actual dissipated power vs. position within the tissue, it is useful for verifying that the power is well confined, does not generate large standing waves in the tissue or sample holder and dissipates rapidly and totally within the tissue at all frequencies. It also shows that we have a maximum power density (highest SAR) at a position that is both a function of the frequency dependent absorption coefficient as well as the refractive index – which is highest at the lower end of the 5G bands and causes significant focusing inside the sample. Our waveguide delivery system, like open air 5G antennas, does not deliver a pure plane wave to the tissue, and hence this effect must be considered when evaluating the SAR and heating effects within the tissue.

ACKNOWLEDGEMENTS

The authors thank Dr. Kingman Fung of JPL for the GaN solid state power amplifier used for the bovine brain measurements at 39 GHz and Professor Ali Hajimiri of Caltech for the AR traveling wave tube power amplifiers used for the 1.9, 4, 29 and 39 GHz gel and the 1.9 and 4 GHz bovine brain measurements. They would like to thank JPL's David Steinfeld for use of the Keysight probe system for measuring the dielectric constants of the brain and gel samples.

REFERENCES

[1] *Millimeter Wave Propagation: Spectrum Management Implications*, Federal Commun. Commission (FCC), Office Eng. Technol. (OET), New Technol. Develop. Division, Washington, DC, USA, Jul. 1997, p. 26.

[2] *Measuring Digital Development, Facts and Figures 2019*, Int. Telecommun. Union (ITU), ITU Publications, Geneva, Switzerland, 2019, p. 14.

[3] J. C. Gallagher and M. E. DeVine, *Fifth Generation (5G) Telecommunications Technologies: Issues for Congress*, document R45485, Congressional Research Service Report, Jan. 2019. [Online]. Available: https://crsreports.congress.gov

[4] D. Abecassis, J. Stewart, and C. Nickerson, "Global Race to 5G—Update," Final Rep. Cellular Telecommun. Internet Assoc. (CTIA), Washington, DC, USA, Tech. Rep. 2015448-103, Apr. 2019, p. 172.

[5] M. Medin and G. Louie, "The 5G ecosystem: Risks and opportunities for DoD," Defense Innov. Board, Dept. Defense, Washington, DC, USA, Tech. Rep. DIB 5G Study, Apr. 2019, p. 33.

[6] M. Marcus and B. Pattan, "Millimeter wave propagation: Spectrum management implications," *IEEE Microw. Mag.*, vol. 6, no. 2, pp. 54–62, Jun. 2005.

[7] K. Gritton, C. Ho, and R. Crane, *Ka-Band Propagation Model Based on High Resolution Acts Data*, document JPL D-30175, NASA-Jet Propulsion Laboratory, Aug. 2004, p. 138.

[8] E. K. Smith, "Centimeter and millimeter wave attenuation and brightness temperature due to atmospheric oxygen and water vapor," *Radio Sci.*, vol. 17, no. 6, pp. 1455–1464, Nov. 1982, doi: 10.1029/RS017i006p01455.

[9] E. Björnson, L. Sanguinetti, H. Wymeersch, J. Hoydis, and T. L. Marzetta, "Massive MIMO is a reality–what is next?" *Digit. Signal Process.*, vol. 94, pp. 3–20, Nov. 2019, doi: 10.1016/j.dsp.2019.06.007.

[10] *2019 Broadband Deployment Report*, Federal Commun. Commission (FCC), Federal Commun. Commission (FCC), FCC 19-44, Washington, DC, USA, May 2019, p. 331.

[11] D. L. Means and K. W. Chan, *Evaluating Compliance with FCC Guidelines for Human Exposure to Radio frequency Electromagnetic Fields, Additional Information for Evaluating Compliance With Mobile and Portable Devices With FCC Limits for Human Exposure to Radiofrequency Emissions, ET Bulletin 65, Supplement C*, Federal Commun. Commission (FCC), Office Eng. Technol., Washington, DC, USA, Jun. 2001, p. 57.

[12] R. Saunders, E. van Rongen, and E. van Deventer, *WHO Research Agenda for Radiofrequency Fields*. Geneva, Switzerland: World Health Organization (WHO), Office of Press and Public Relations, 2010, p. 42.

[13] E. R. Adair and R. C. Petersen, "Biological effects of radiofrequency/microwave radiation," *IEEE Trans. Microw. Theory Techn.*, vol. 50, no. 3, pp. 953–962, Mar. 2002.

[14] J. M. Osepchuk and R. C. Petersen, "Historical review of RF exposure standards and the international committee on electromagnetic safety (ICES)," *Bioelectromagnetics*, vol. 24, no. S6, pp. S7–S16, 2003, doi: 10.1002/bem.10150.
[15] A. Vander Vorst, A. Rosen, and Y. Kotsuka, *RF/Microwave Interaction with Biological Tissues*. Hoboken, NJ, USA: Wiley, 2006.
[16] C. K. Chou, H. Bassen, J. Osepchuk, Q. Balzano, R. Petersen, M. Meltz, R. Cleveland, J. C. Lin, and L. Heynick, "Radio frequency electromagnetic exposure: Tutorial review on experimental dosimetry," *Bioelectromagnetics*, vol. 17, no. 3, pp. 195–208, 1996.
[17] A. W. Guy, M. D. Webb, and C. C. Sorensen, "Determination of power absorption in man exposed to high frequency electromagnetic fields by thermographic measurements on scale models," *IEEE Trans. Biomed. Eng.*, vol. BME-23, no. 5, pp. 361–370, Sep. 1976, doi: 10.1109/tbme.1976.324645.
[18] K. J. Oscar and T. D. Hawkins, "Microwave alteration of the blood-brain barrier system of rats," *Brain Res*, vol. 126, no. 2, pp. 281–293, May 1977, doi: 10.1016/0006-8993(77)90726-0.
[19] O. P. Gandhi, "Dosimetry—The absorption properties of man and experimental animals," *Bull. New York Acad. Med.*, vol. 55, no. 11, pp. 999–1020, Dec. 1979.
[20] W. G. Lotz and R. P. Podgorski, "Temperature and adrenocortical responses in rhesus monkeys exposed to microwaves," *J. Appl. Physiol.*, vol. 53, no. 6, pp. 1565–1571, Dec. 1982, doi: 10.1152/jappl.1982.53.6.1565.
[21] A. H. Frey, "Studies of the blood-brain barrier: Preliminary findings and discussion," *Radio Sci.*, vol. 14, no. 6S, pp. 349–350, Nov. 1979, doi: 10.1029/RS014i06Sp00349.
[22] J. G. Burr and J. H. Krupp, "Real-time measurement of RFR energy distribution in the macaca mulatta head," *Bioelectromagnetics*, vol. 1, no. 1, pp. 21–34, 1980, doi: 10.1002/bem.2250010103.
[23] J. R. Thomas, J. Schrot, and R. A. Banvard, "Comparative effects of pulsed and continuous-wave 2.8-GHz microwaves on temporally defined behavior," *Bioelectromagnetics*, vol. 3, no. 2, pp. 227–235, 1982, doi: 10.1002/bem.2250030207.
[24] R. G. Olsen, "Far-field dosimetric measurements in a full-sized man model at 2.0 GHz," *Bioelectromagnetics*, vol. 3, no. 4, pp. 433–441, 1982, doi: 10.1002/bem.2250030406.
[25] W. G. Lotz, "Hyperthermia in radiofrequency-exposed rhesus monkeys: A comparison of frequency and orientation effects," *Radiat. Res.*, vol. 102, no. 1, pp. 59–70, Apr. 1985.
[26] M. R. Frei and J. R. Jauchem, "Thermoregulatory responses of rats exposed to 9.3-GHz microwaves—A comparison of E-orientation and H-orientation," *Physiol. Chem. Phys. Med.*, vol. 24, no. 1, pp. 1–10, 1992.
[27] J. A. D'Andrea, A. Thomas, and D. J. Hatcher, "Rhesus monkey behavior during exposure to high-peak-power 5.62-GHz microwave pulses," *Bioelectromagnetics*, vol. 15, no. 2, pp. 76–163, 1994, doi: 10.1002/bem.2250150207.
[28] E. R. Adair, B. L. Cobb, K. S. Mylacraine, and S. A. Kelleher, "Human exposure at two radio frequencies (450 and 2450 MHz): Similarities and differences in physiological response," *Bioelectromagnetics*, vol. 20, no. S4, pp. 12–20, 1999.
[29] K. L. Ryan, J. A. D'Andrea, J. R. Jauchem, and P. A. Mason, "Radio frequency radiation of millimeter wave length: Potential occupational safety issues relating to surface heating," *Health Phys.*, vol. 78, no. 2, pp. 170–181, Feb. 2000, doi: 10.1097/00004032-200002000-00006.
[30] J. M. Ziriax, K. I. Smith, D. A. Nelson, K. L. Ryan, P. Gajsek, J. A. D'Andrea, T. J. Walters, W. D. Hurt, and P. A. Mason, "Effects of frequency, permittivity, and voxel size on predicted specific absorption rate values in biological tissue during electromagnetic-field exposure," *IEEE Trans. Microw. Theory Techn.*, vol. 48, no. 11, pp. 2050–2058, Nov. 2000.
[31] E. R. Adair, K. S. Mylacraine, and B. L. Cobb, "Partial-body exposure of human volunteers to 2450 MHz pulsed or CW fields provokes similar thermoregulatory responses," *Bioelectromagnetics*, vol. 22, no. 4, pp. 246–259, May 2001, doi: 10.1002/bem.47.
[32] D. A. Nelson, T. J. Walters, K. L. Ryan, K. B. Emerton, W. D. Hurt, M. J. Ziriax, L. R. Johnson, and P. A. Mason, "Inter-species extrapolation of skin heating resulting from millimeter wave irradiation: Modeling and experimental results," *Health Phys.*, vol. 84, no. 5, pp. 608–615, May 2003, doi: 10.1097/00004032-200305000-00006.
[33] L. G. Salford, H. Nittby, A. Brun, G. Grafström, L. Malmgren, M. Sommarin, J. Eberhardt, B. Widegren, and B. R. R. Persson, "The mammalian brain in the electromagnetic fields designed by man with special reference to blood-brain barrier function, neuronal damage and possible physical mechanisms," *Prog. Theor. Phys. Suppl.*, vol. 173, pp. 283–309, Jan. 2008.
[34] M. Blank and R. Goodman, "Electromagnetic fields stress living cells," *Pathophysiology*, vol. 16, nos. 2–3, pp. 71–78, Aug. 2009, doi: 10.1016/j.pathophys.2009.01.006.
[35] J. L. Phillips, N. P. Singh, and H. Lai, "Electromagnetic fields and DNA damage," *Pathophysiology*, vol. 16, nos. 2–3, pp. 79–88, Aug. 2009, doi: 10.1016/j.pathophys.2008.11.005.
[36] S. Roggeveen, J. van Os, and R. Lousberg, "Does the brain detect 3G mobile phone radiation peaks? An explorative in-depth analysis of an experimental study," *PLoS ONE*, vol. 10, no. 5, May 2015, Art. no. e0125390, doi: 10.1371/journal.pone.0125390.
[37] A. Şahin, A. Aslan, O. BaŞ, A. Ikinci, C. Özyılmaz, O. Fikret Sönmez, S. Çolakoğlu, and E. Odacı, "Deleterious impacts of a 900-MHz electromagnetic field on hippocampal pyramidal neurons of 8-week-old sprague Dawley male rats," *Brain Res.*, vol. 1624, pp. 232–238, Oct. 2015, doi: 10.1016/j.brainres.2015.07.042.
[38] Z. Sienkiewicz and E. van Rongen, "Can low-level exposure to radiofrequency fields effect cognitive behaviour in laboratory animals? A systematic review of the literature related to spatial learning and place memory," *Int. J. Environ. Res. Public Health*, vol. 16, no. 9, p. 1607, May 2019, doi: 10.3390/ijerph16091607.
[39] I. Commission on Non-Ionizing Radiation Protection (ICNIRP)1, "Guidelines for limiting exposure to electromagnetic fields (100 kHz to 300 GHz)," *Health Phys.*, vol. 118, no. 5, pp. 483–524, May 2020. [Online]. Available: https://journals.lww.com/health-physics/Fulltext/publishahead/Guidelines_for_Limiting_Exposure_to.99797.aspx.
[40] *IEEE Standard for Safety Levels With Respect to Human Exposure to Electric, Magnetic, and Electromagnetic Fields, 0 Hz to 300 GHz*, IEEE Standard C95.1-2019 (Revision of IEEE Standard C95.1-2005/ Incorporates IEEE Standard C95.1-2019/Cor 1-2019), Oct. 2019, pp. 1–312, doi: 10.1109/IEEESTD.2019.8859679.
[41] *IEEE Recommended Practice for Determining the Peak Spatial-Average Specific Absorption Rate (SAR) in the Human Head From Wireless Communications Devices: Measurement Techniques*, IEEE Standard 1528-2013 (Revision IEEE Standard 1528-2003), Sep. 2013, pp. 1–246, doi: 10.1109/IEEESTD.2013.6589093.
[42] *IEEE Recommended Practice for Measurements and Computations of Radio Frequency Electromagnetic Fields With Respect to Human Exposure to Such Fields, 100 kHz-300 GHz*, IEEE Standard C95.3-2002 (Revision IEEE Standard C95.3-1991), 2002, pp. 1–126.
[43] D. Belpomme, L. Hardell, I. Belyaev, E. Burgio, and D. O. Carpenter, "Thermal and non-thermal health effects of low intensity non-ionizing radiation: An international perspective," *Environ. Pollut.*, vol. 242, pp. 643–658, Nov. 2018, doi: 10.1016/j.envpol.2018.07.019.
[44] F. S. Barnes, "Mechanisms for electric and magnetic fields effects on biological cells," *IEEE Trans. Magn.*, vol. 41, no. 11, pp. 4219–4224, Nov. 2005, doi: 10.1109/Tmag.2005.855480.
[45] D. H. Gultekin and J. C. Gore, "Temperature dependence of nuclear magnetization and relaxation," *J. Magn. Reson.*, vol. 172, no. 1, pp. 133–141, Jan. 2005, doi: 10.1016/j.jmr.2004.09.007.
[46] N. D. Volkow, D. Tomasi, G.-J. Wang, P. Vaska, J. S. Fowler, F. Telang, D. Alexoff, J. Logan, and C. Wong, "Effects of cell phone radiofrequency signal exposure on brain glucose metabolism," *J. Amer. Med. Assoc.*, vol. 305, no. 8, pp. 808–813, Feb. 2011, doi: 10.1001/jama.2011.186.
[47] D. H. Gultekin and L. Moeller, "NMR imaging of cell phone radiation absorption in brain tissue," *Proc. Nat. Acad. Sci. USA*, vol. 110, no. 1, pp. 58–63, Jan. 2013, doi: 10.1073/pnas.1205598109.
[48] M. W. Dewhirst, B. L. Viglianti, M. Lora-Michiels, M. Hanson, and P. J. Hoopes, "Basic principles of thermal dosimetry and thermal thresholds for tissue damage from hyperthermia," *Int. J. Hyperthermia*, vol. 19, no. 3, pp. 267–294, Jan. 2003, doi: 10.1080/0265673031000119006.
[49] G. C. van Rhoon, T. Samaras, P. S. Yarmolenko, M. W. Dewhirst, E. Neufeld, and N. Kuster, "CEM43°C thermal dose thresholds: A potential guide for magnetic resonance radiofrequency exposure levels?" *Eur. Radiol.*, vol. 23, no. 8, pp. 2215–2227, Aug. 2013, doi: 10.1007/s00330-013-2825-y.
[50] D. H. Gultekin and J. C. Gore, "Measurement of specific heat and specific absorption rate by nuclear magnetic resonance," *Thermochimica Acta*, vols. 503–504, pp. 100–107, May 2010, doi: 10.1016/j.tca.2010.03.015.
[51] D. H. Gultekin and J. C. Gore, "Simultaneous measurements of thermal conductivity, thermal diffusivity and specific heat by nuclear magnetic resonance imaging," *Thermochimica Acta*, vol. 519, nos. 1–2, pp. 96–102, May 2011, doi: 10.1016/j.tca.2011.02.041.

[52] L. Alon, D. K. Sodickson, and C. M. Deniz, "Heat equation inversion framework for average SAR calculation from magnetic resonance thermal imaging," *Bioelectromagnetics*, vol. 37, no. 7, pp. 493–503, Oct. 2016, doi: 10.1002/bem.21996.

[53] K. R. Foster, J. L. Schepps, R. D. Stoy, and H. P. Schwan, "Dielectric properties of brain tissue between 0.01 and 10 GHz," *Phys. Med. Biol.*, vol. 24, no. 6, pp. 1177–1187, Nov. 1979, doi: 10.1088/0031-9155/24/6/008.

[54] C. Gabriel, "Compilation of the dielectric properties of body tissues at RF and microwave frequencies," Armstrong Lab., Occupational Environ. Health Directorate, Radiofrequency Radiat. Division, Brooks Air Force Base, San Antonio, TX, USA, Tech. Rep. AL/OE-TR-1996-0037, 1996.

[55] M. C. Steel and R. J. Sheppard, "Dielectric properties of mammalian brain tissue between 1 and 18 GHz," *Phys. Med. Biol.*, vol. 30, no. 7, pp. 621–630, Jul. 1985, doi: 10.1088/0031-9155/30/7/001.

[56] G. Schmid, G. Neubauer, and P. R. Mazal, "Dielectric properties of human brain tissue measured less than 10 h postmortem at frequencies from 800 to 2450 MHz," *Bioelectromagnetics*, vol. 24, no. 6, pp. 423–430, Sep. 2003, doi: 10.1002/bem.10123.

[57] N. Kuster, V. Santomaa, and A. Drossos, "The dependence of electromagnetic energy absorption upon human head tissue composition in the frequency range of 300-3000 MHz," *IEEE Trans. Microw. Theory Techn.*, vol. 48, no. 11, pp. 1988–1995, Nov. 2000, doi: 10.1109/22.884187.

[58] A. Hirata, S.-I. Matsuyama, and T. Shiozawa, "Temperature rises in the human eye exposed to EM waves in the frequency range 0.6-6 GHz," *IEEE Trans. Electromagn. Compat.*, vol. 42, no. 4, pp. 386–393, 4th Quart., 2000, doi: 10.1109/15.902308.

[59] A. Hirata and O. Fujiwara, "The correlation between mass-averaged SAR and temperature elevation in the human head model exposed to RF near-fields from 1 to 6 GHz," *Phys. Med. Biol.*, vol. 54, no. 23, pp. 7227–7238, Dec. 2009, doi: 10.1088/0031-9155/54/23/013.

[60] M. C. Ziskin, S. I. Alekseev, K. R. Foster, and Q. Balzano, "Tissue models for RF exposure evaluation at frequencies above 6 GHz," *Bioelectromagnetics*, vol. 39, no. 3, pp. 173–189, Apr. 2018, doi: 10.1002/bem.22110.

[61] R. Morimoto, A. Hirata, I. Laakso, M. C. Ziskin, and K. R. Foster, "Time constants for temperature elevation in human models exposed to dipole antennas and beams in the frequency range from 1 to 30 GHz," *Phys. Med. Biol.*, vol. 62, no. 5, pp. 1676–1699, Mar. 2017, doi: 10.1088/1361-6560/aa5251.

[62] K. R. Foster, M. C. Ziskin, Q. Balzano, and A. Hirata, "Thermal analysis of averaging times in radio-frequency exposure limits above 1 GHz," *IEEE Access*, vol. 6, pp. 74536–74546, 2018, doi: 10.1109/ACCESS.2018.2883175.

[63] D. Funahashi, A. Hirata, S. Kodera, and K. R. Foster, "Area-averaged transmitted power density at skin surface as metric to estimate surface temperature elevation," *IEEE Access*, vol. 6, pp. 77665–77674, 2018, doi: 10.1109/ACCESS.2018.2883733.

[64] S. Kodera, A. Hirata, D. Funahashi, S. Watanabe, K. Jokela, and R. J. Croft, "Temperature rise for brief radio-frequency exposure below 6 GHz," *IEEE Access*, vol. 6, pp. 65737–65746, 2018, doi: 10.1109/ACCESS.2018.2878149.

[65] T. Nakae, D. Funahashi, J. Higashiyama, T. Onishi, and A. Hirata, "Skin temperature elevation for incident power densities from dipole arrays at 28 GHz," *IEEE Access*, vol. 8, pp. 26863–26871, 2020, doi: 10.1109/ACCESS.2020.2970219.

[66] R. Morimoto, I. Laakso, V. De Santis, and A. Hirata, "Relationship between peak spatial-averaged specific absorption rate and peak temperature elevation in human head in frequency range of 1–30 GHz," *Phys. Med. Biol.*, vol. 61, no. 14, pp. 5406–5425, Jul. 2016, doi: 10.1088/0031-9155/61/14/5406.

[67] K. Sasaki, M. Mizuno, K. Wake, and S. Watanabe, "Monte Carlo simulations of skin exposure to electromagnetic field from 10 GHz to 1 THz," *Phys. Med. Biol.*, vol. 62, no. 17, pp. 6993–7010, Aug. 2017, doi: 10.1088/1361-6560/aa81fc.

[68] S. Kodera, J. Gomez-Tames, and A. Hirata, "Temperature elevation in the human brain and skin with thermoregulation during exposure to RF energy," *Biomed. Eng. OnLine*, vol. 17, no. 1, Dec. 2018, doi: 10.1186/s12938-017-0432-x.

[69] D. H. Gultekin and J. C. Gore, "Measurement of heat transfer coefficients by nuclear magnetic resonance," *Magn. Reson. Imag.*, vol. 26, no. 9, pp. 1323–1328, Nov. 2008, doi: 10.1016/j.mri.2008.04.006.

[70] D. H. Gultekin and J. C. Gore, "Measurement of thermal diffusivity by magnetic resonance imaging," *Magn. Reson. Imag.*, vol. 24, no. 9, pp. 1203–1207, Nov. 2006, doi: 10.1016/j.mri.2006.03.014.

[71] O. P. Gandhi, "Frequency and orientation effects on whole animal absorption of electromagnetic waves," *IEEE Trans. Biomed. Eng.*, vol. BME-22, no. 6, pp. 536–542, Nov. 1975, doi: 10.1109/tbme.1975.324479.

[72] N. Kuster, V. B. Torres, N. Nikoloski, M. Frauscher, and W. Kainz, "Methodology of detailed dosimetry and treatment of uncertainty and variations for *in vivo* studies," *Bioelectromagnetics*, vol. 27, no. 5, pp. 378–391, Jul. 2006, doi: 10.1002/bem.20219.

[73] N. Kuster and Q. Balzano, "Energy absorption mechanism by biological bodies in the near field of dipole antennas above 300 MHz," *IEEE Trans. Veh. Technol.*, vol. 41, no. 1, pp. 17–23, Feb. 1992, doi: 10.1109/25.120141.

[74] R. L. Mcintosh and V. Anderson, "A comprehensive tissue properties database provided for the thermal assessment of a human at rest," *Biophys. Rev. Lett.*, vol. 5, no. 3, pp. 129–151, Sep. 2010, doi: 10.1142/S1793048010001184.

[75] P. A. Bottomley and E. R. Andrew, "RF magnetic field penetration, phase shift and power dissipation in biological tissue: Implications for NMR imaging," *Phys. Med. Biol.*, vol. 23, no. 4, pp. 630–643, Jul. 1978, doi: 10.1088/0031-9155/23/4/006.

[76] T. Vaughan, L. DelaBarre, C. Snyder, J. Tian, C. Akgun, D. Shrivastava, W. Liu, C. Olson, G. Adriany, J. Strupp, P. Andersen, A. Gopinath, P.-F. van de Moortele, M. Garwood, and K. Ugurbil, "9.4T human MRI: Preliminary results," *Magn. Reson. Med.*, vol. 56, no. 6, pp. 1274–1282, Dec. 2006, doi: 10.1002/mrm.21073.

[77] P. A. Bottomley, "Turning up the heat on MRI," *J. Amer. College Radiol.*, vol. 5, no. 7, pp. 853–855, Jul. 2008, doi: 10.1016/j.jacr.2008.04.003.

[78] H. H. Pennes, "Analysis of tissue and arterial blood temperatures in the resting human forearm," *J. Appl. Physiol.*, vol. 1, no. 2, pp. 93–122, Aug. 1948, doi: 10.1152/jappl.1948.1.2.93.

[79] H. S. Carslaw and J. C. Jaeger, *Conduction of Heat in Solids*, 2nd ed. Oxford, U.K.: Clarendon, 1986, p. 510.

[80] *Council Recommendation of 12 July 1999 on the Limitation of Exposure of the General Public to Electromagnetic Fields (0 Hz to 300 GHz)*, Off. J. Eur. Communities, Council Eur. Union, Brussels, Belgium, Jul. 1999, vol. L 199/59, no. 59.

DAVID H. GULTEKIN received the B.S. degree from Istanbul Technical University, Turkey, and the M.S. degree from the Stevens Institute of Technology, Hoboken, NJ, USA, all in materials science and engineering, and the M.S. degree in applied science and engineering, and the M.Phil. and Ph.D. degrees in electrical engineering from Yale University, New Haven, CT, USA. He has completed a Graduate Program in materials science and engineering at the Massachusetts Institute of Technology, Cambridge, MA, USA. He held a postdoctoral and fellowship positions in radiation oncology, physics and biology, and radiology and radiological sciences at Duke University, Durham, NC, USA, California Institute of Technology, Pasadena, CA, USA, and Johns Hopkins University, Baltimore, MD, USA. He held faculty positions at the Memorial Sloan-Kettering Cancer Center and the Cornell Medical College, where he had joint appointments as an Assistant Professor. He also conducted research at the Cedars-Sinai Medical Center. He provided a broad range of physics and engineering expertise for cancer imaging and participated in multi-institutional clinical trials for the assessment of response to radiation, chemical cytotoxic, and targeted therapies such as monoclonal antibodies and anti-angiogenic therapies. He developed methods and algorithms for processing large radiological datasets to enhance clinical practice and research. He investigated MRI techniques to measure mass and energy transport processes with high spatial and temporal resolutions and developed MRI methods for measuring thermal diffusivity, thermal conductivity, heat transfer coefficients, specific heat, specific absorption rate, thermal power, and the heat of reaction in substances noninvasively. He currently conducts research with Columbia University, New York City, NY, USA, in magnetic resonance imaging and spectroscopy, radiofrequency absorption in substances, and NMR thermometry. He also serves as the MRI Safety Officer of Columbia University.

PETER H. SIEGEL (Life Fellow, IEEE) received the B.A. degree in astronomy from Colgate University, in 1976, the M.S. degree in physics from Columbia University, in 1978, and the Ph.D. degree in electrical engineering (EE) from Columbia University, in 1983. He has held appointments as a Research Fellow and an Engineering Staff at the NASA Goddard Institute for Space Studies, New York City, NY, USA, from 1975 to 1983, a Staff Scientist at the National Radio Astronomy Observatory, Central Development Labs, Charlottesville, VA, USA, from 1984 to1986, a Technical Group Supervisor and a Senior Research Scientist at the Jet Propulsion Laboratory (JPL), National Aeronautics and Space Administration (NASA), Pasadena, CA, USA, from 1987 to 2014, and a Faculty Associate in electrical engineering and a Senior Scientist in biology at the California Institute of Technology (Caltech), Pasadena, CA, USA, from 2002 to 2014. At JPL, he founded and led the Submillimeter Wave Advanced Technology (SWAT) Team, that is, a group of 20+ scientists and engineers developing THz technology for NASA's near and long-term space missions, for 25 years. This included delivering key components for four major satellite missions and leading more than 75 smaller Research and Development programs for NASA and the U.S. Department of Defense. At Caltech, he was involved in new biological and medical applications of THz, especially low-power effects on neurons and most recently millimeter-wave monitoring of blood chemistry. He has served as an IEEE Distinguished Lecturer, and the Vice-Chair and Chair of the IEEE MTTS THz Technology Committee. He is currently an Elected Member of the MTTS AdCom. Dr. Siegel has published more than 300 articles on THz components and technology and has given more than 250 invited talks on this subject throughout his career of 45 years in THz. His current appointments include the CEO of THz Global, a small Research and Development company specializing in RF bio applications, a Senior Scientist Emeritus of biology and electrical engineering with Caltech, and a Senior Research Scientist Emeritus and a Principal Engineer with the NASA Jet Propulsion Laboratory. Dr. Siegel has been recognized with 75 NASA technology awards, ten NASA team awards, the NASA Space Act Award, three individual JPL awards for technical excellence and four JPL team awards, and the IEEE MTTS Applications Award, in 2018. He is honored to take up the responsibility as the Founding Editor-in-Chief for a new open access publication: IEEE Journal of Microwaves, with expected inaugural issue release date of January 2021. Among many other functions, he served as the Founding Editor-in-Chief for the IEEE Transactions on Terahertz Science and Technology, from 2010 to 2015, and the founder, in 2009, Chair through 2011, and elected General Secretary since 2012, of the International Society of Infrared, Millimeter, and Terahertz Waves (IRMMW-THz), the world's largest society devoted exclusively to THz science and technology.